3 Optical Properties of ZnO and Related Compounds

C. Bundesmann, R. Schmidt-Grund, and M. Schubert

In this chapter some of the presently known optical properties of zinc oxide are reviewed. In particular, the anisotropic dielectric functions (DFs) of ZnO and related compounds from the far-infrared (FIR) to the vacuum-ultraviolet (VUV) spectral range are studied. Thereupon, many fundamental physical parameters can be derived, such as the optical phonon-mode frequencies and their broadening values, the free-charge-carrier parameters, the static and "high-frequency" dielectric constants, the dispersion of the indices of refraction within the band-gap region, the fundamental and above-band-gap band-to-band transition energies and their excitonic contributions.

3.1 Introduction

ZnO has regained much interest because of a large variety of properties, which make ZnO superior to currently used materials. For instance, ZnO-based alloys might become alternative materials for GaN-based alloys, which are currently used in ultraviolet (UV) optoelectronic devices. The fundamental band gap energy of ZnO is similar to that of GaN, but the ground-state exciton binding energy of ZnO is more than two times larger than that of GaN (Table 3.1). Hence, stimulated excitonic emission even above room temperature (RT) is possible in ZnO, but not in GaN. ZnO-based laser devices with low threshold currents operating above RT are quite likely [1]. In fact, optically pumped lasing at RT was already demonstrated by several groups [1–5].

Upon alloying with MgO or CdO, the fundamental band gap of ZnO can be shifted to higher or lower energies, respectively (Table 3.1) [11–16]. Furthermore, the electrical n-type conductivity of ZnO can be controlled over many orders of magnitude by doping with Al or Ga [17–20]. On the other hand, reproducible p-type conductivity in ZnO is still a challenge. Doping with group-I elements (Li, Na, K, etc.), which are supposed to substitute the Zn-atoms, or doping with group-V elements (N, P, As, Sb, etc.), which are supposed to substitute the O-atoms, are promising pathways toward p-type conductivity [18, 21, 22]. Upon alloying with Mn or other transition metals, ZnO can reveal ferromagnetic properties with a Curie temperature above RT [23–28]. Essential for the performance of the above addressed materials is the knowledge of fundamental properties.

Table 3.1. Band-gap energy E_g and the (ground state) exciton binding energy E_{xb}^1 of ZnO, GaN, MgO, and CdO

		ZnO		GaN		MgO		CdO	
E_g	(eV)	3.37	[6]	3.30	[7]	7.6	[8]	2.3	[9]
E_{xb}^1	(meV)	60	[10]	18–28	[7]	80	[8]	–	

By evaluation of the phonon-mode frequencies, information about strain [29] or about the incorporation of doping or alloying atoms can be derived. Besides the phonon-mode frequency, the phonon-mode broadening parameter provides information about crystal quality [30], because scattering due to a lower crystal quality or due to alloying makes the phonon-mode broadening parameter larger.

Plasmons – the collective free-charge-carrier modes – interact with the longitudinal phonons, when the screened plasma frequency ω_p is in the frequency range of the optical phonons. Thereupon, coupled phonon–plasmon modes are formed. In principle, both Raman scattering and infrared (IR) spectroscopic techniques are able to detect these modes. Unfortunately, the Raman scattering intensity of the uncoupled longitudinal phonon modes of ZnO is weak [31], such that the coupled modes cannot be detected. In contrast to that, IR spectroscopic techniques, for instance infrared spectroscopic ellipsometry (IRSE), can clearly reveal the plasmon-mode contributions to the DFs, and the free-charge-carrier properties can be quantified. For highly-conductive ZnO the plasma frequency moves from the mid-IR into the near-IR or even into the visible spectral region. Therefore, spectroscopic techniques in the near-IR and visible spectral region are more appropriate for studying the free-charge-carrier parameters in highly-conductive ZnO thin film samples (see paragraph *optical properties* in Sects. 6.2.5.2, p. 273 and 8.3.1, Fig. 8.13).

The DFs of ZnO reveal a complex behavior in the vicinity of the fundamental band gap energy, as well as for photon energies above the band gap energy, where multiple electronic transitions occur, dispersed over wide regions of the Brillouin zone. The unambiguous assignment of type, symmetry, and location of a given transition within the Brillouin zone can only be done in conjunction with theoretical band structure analysis, except for the lowest Γ-point transitions. Here, experimentally observed DF spectra are discussed, as well as their analysis in terms of critical point (CP) structures and associated band-to-band transitions without attempting to connect those to individual symmetry points. The fundamental band gap energy E_g is the lowest energy, at which absorption sets in. It can be determined, for instance, by transmission measurements. In ZnO, a semiconductor with dipole-allowed direct band-to-band transitions, excitons couple strongly to the radiation field, and their absorption lines are superimposed onto the CP structures because of the band-to-band transitions. Homogeneous and inhomogeneous broadening effects smear out the absorption features, giving rise to a wide range of reported E_g values, in addition to intrinsic origins for energy shifts,

such as impurities, strain, composition variations, etc. Spectroscopic ellipsometry (SE) can be used to separate excitonic contributions from band-to-band transitions and for their quantitative assessment.

Further attention is paid to the temperature-dependencies of phonon modes, indices of refraction, and fundamental-band-gap energies.

Wurtzite-structure ZnO thin films grown by a variety of deposition techniques, as well as commercially available single crystal bulk samples are discussed. Furthermore, data for ZnO thin films intermixed with numerous elements are reviewed. Most of the results are obtained by SE, which is a precise and reliable tool for measurements of the DFs. The SE results are supplemented by Raman scattering and electrical Hall-effect measurement data, as well as data reported in the literature by similar or alternative techniques (reflection, transmission, and luminescence excitation spectroscopy).

Raman scattering was often applied for studying the phonon modes of ZnO bulk samples [31–38]. It has become a fast and reliable tool to study ZnO thin films [29, 38–43], and ZnO nano- and/or microstructures [44–46]. Raman scattering studies were also reported for ZnO samples doped with Li [43, 47, 48], N [43, 49–51], Al [48, 52–54], P [43, 55], Mn [43, 56–58], Fe [43, 48], Co [43], Ni [43], Cu [43], Ga [48, 51], As [59], Ce [60], or Sb [48, 61], and $(Mg,Cd)_xZn_{1-x}O$ [43, 62] samples. IR reflection [63–65] and transmission measurements [66–68] were reported mainly for ZnO bulk materials. IR optical studies of doped ZnO and ZnO-based thin films are, in general, restricted to transmission and reflection measurements in the near-IR (NIR) spectral region, and to highly conductive Al-doped ZnO thin films. Some experiments were performed in the mid-IR (MIR) spectral region [52, 69, 70], where the optical phonon modes can be studied. Recently, IRSE was applied to study undoped and doped ZnO films, and ZnO-based alloy films [30, 38, 43, 62, 71–74].

The number of spectroscopic studies of ZnO and related materials in the spectral region around the fundamental band gap is too large to be listed here. Undoped and doped ZnO as well as ZnO-based alloy samples were studied by photoluminescence (PL), transmission and reflection measurements (see review articles [6,75]). Also, SE measurements were reported for ZnO [76–85] and related materials, for instance, metal-doped ZnO [70,86–89], $Mg_xZn_{1-x}O$ [15, 16, 82, 90, 91], $Co_xZn_{1-x}O$ [92], $Mn_xZn_{1-x}O$ [93], or $Fe_xZn_{1-x}O$ [94].

3.2 Basic Concepts and Properties

3.2.1 Structural Properties

Undoped and doped ZnO, and most of the ZnO-based alloys crystallize under normal conditions in the wurtzite structure, but ZnO-based alloys can reveal a rocksalt structure for a high content of alloying atoms. One example is Mg-rich $Mg_xZn_{1-x}O$. Thus, a phase transition with change of coordination

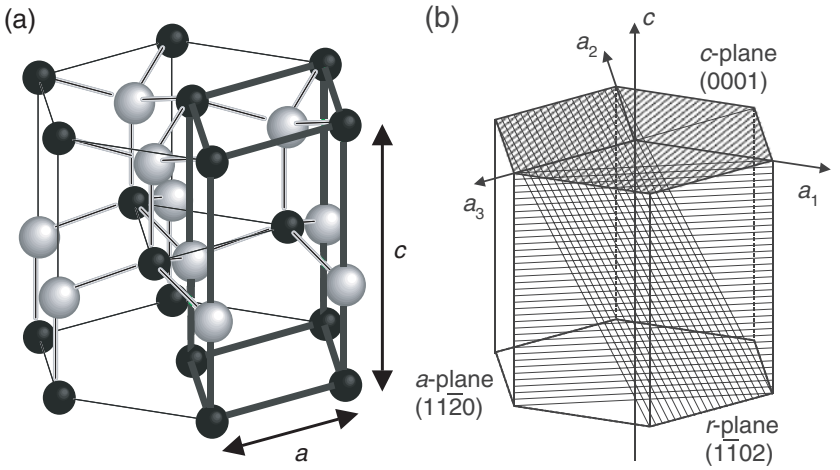

Fig. 3.1. (**a**) Primitive cell (*heavy lines*) of the wurtzite-structure lattice placed within a hexagonal prism. a and c are the lattice constants. (**b**) Schematic drawing of surfaces cut from a hexagonal single crystal with different crystallographic orientations (*surface planes*)

must occur, which affects many physical properties. The phase transition for PLD-grown $Mg_xZn_{1-x}O$ thin films was observed in the composition range between 53% and 68% Mg content, whereas scattered reports exist on more diffuse transition regions for other $Mg_xZn_{1-x}O$ samples [11, 14–16, 82, 90, 91, 95–100].

3.2.1.1 Wurtzite Crystal Structure (Hexagonal)

The wurtzite crystal structure belongs to the hexagonal system with space group C_{6v}^4 ($P6_3mc$) in the Schoenflies (short standard) notation. Two atom species occupy the positions of a closest packed hexagonal lattice each. These two sublattices are shifted along the c-axis against each other (Fig. 3.1 a). The wurtzite-structure lattice is fourfold coordinated. That is, each atom has four nearest neighbor atoms. Figure 3.1b shows the cuts of different orientations of a crystal with hexagonal structure.[1]

[1] A sample is called "c-plane oriented" or shortly "c-plane," when the investigated surface is the hexagonal (0001)-plane. Analogously, for "a-plane" or "r-plane" samples the investigated surface is the hexagonal (11$\bar{2}$0) or (1$\bar{1}$02) plane, respectively. Wurtzite-structure ZnO and ZnO-based thin films grown on c-plane and a-plane sapphire adopt c-plane orientation, while those grown on r-plane sapphire adopt a-plane orientation [71, 101–104]. (See Sect. 4.2.1 for detailed discussion of ZnO surfaces and see Sect. 1.3, Table 1.1 for further structural parameters).

3.2.1.2 Rocksalt Crystal Structure (Cubic)

The rocksalt crystal structure belongs to the cubic system with space group O_h^1 (Pm3m). It consists of two face-centered cubic (fcc) sublattices, which are occupied by one atom species each. The two sublattices are shifted along one half of the diagonal of the primitive unit cell against each other. The rocksalt lattice is sixfold coordinated.

3.2.2 Vibrational Properties

3.2.2.1 Wurtzite-Structure Phonons

The wurtzite-structure optical phonons at the Γ-point of the Brillouin zone belong to the following irreducible representation [32]

$$\Gamma^{\text{opt}} = 1A_1 + 2B_1 + 1E_1 + 2E_2. \tag{3.1}$$

Hereby, the branches with E_1- and E_2-symmetry are twofold degenerated. Both A_1- and E_1-modes are polar, and split into transverse optical (TO) and longitudinal optical (LO) phonons with different frequencies ω_{TO} and ω_{LO}, respectively, because of the macroscopic electric fields associated with the LO phonons. The short-range interatomic forces cause anisotropy, and A_1- and E_1-modes possess, therefore, different frequencies. The electrostatic forces dominate the anisotropy in the short-range forces in ZnO, such that the TO-LO splitting is larger than the A_1-E_1 splitting. For the lattice vibrations with A_1- and E_1-symmetry, the atoms move parallel and perpendicular to the c-axis, respectively (Fig. 3.2).

Both A_1- and E_1-modes are Raman and IR active. The two nonpolar E_2-modes $E_2^{(1)}$ and $E_2^{(2)}$ are Raman active only. The B_1-modes are IR and Raman inactive (silent modes). Phonon dispersion curves of wurtzite-structure and rocksalt-structure ZnO throughout the Brillouin Zone were reported in [106–108]. For crystals with wurtzite crystal structure, pure longitudinal or

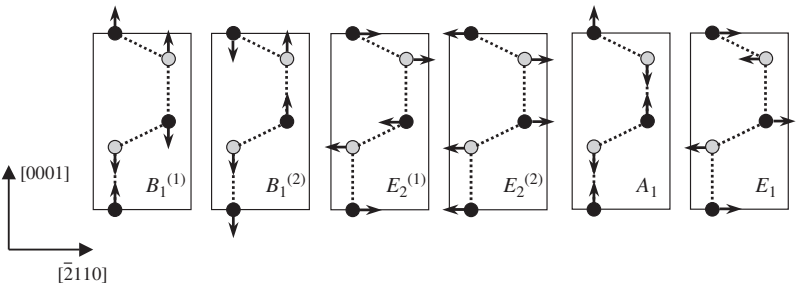

Fig. 3.2. Displacement patterns of the optical phonons of a lattice with wurtzite crystal structure. Reprinted with permission from [105]

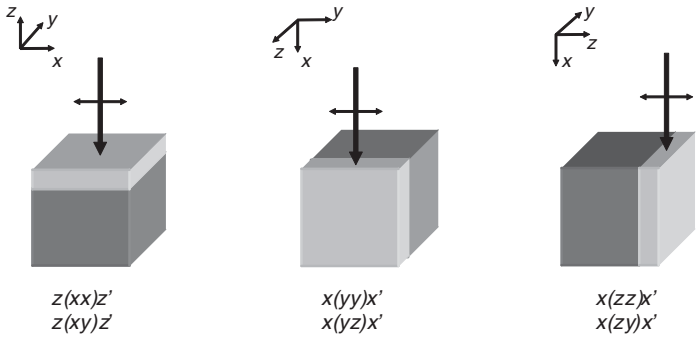

Fig. 3.3. Raman scattering configurations for a thin film on a thick substrate in the backscattering regime. The laboratory coordinate system is chosen such that the z-axis is parallel to the sample normal. The direction and polarization of the incident laser beam are indicated by the vertical arrow and the horizontal double arrow, respectively. By aligning a polarizer within the light path of the scattered light parallel or perpendicular with respect to the polarization direction of the incident laser beam, the two scattering configurations indicated below the drawings can be realized. The notation of the scattering configurations follows the "Porto notation" [32]: The letters before and after the parenthesis show the direction of the incident and scattered light, respectively, while the letters inside the parenthesis indicate the corresponding polarization

pure transverse phonons of well-defined symmetry can be observed only if the phonon propagation is along or perpendicular to the c-axis. Group theory in combination with polarization and propagation considerations allows to identify the symmetry of the Raman active optical modes by applying different scattering configurations [33]. In Fig. 3.3 possible scattering configurations for a thin film on a substrate are drawn schematically.

Table 3.2 summarizes the optical phonons of crystals with wurtzite structure and the scattering configurations, in which the optical phonons are predicted to produce backward signal in first-order Raman scattering.

3.2.2.2 Rocksalt-Structure Phonons

The Γ-point optical phonons of a crystal with rocksalt structure belong to the irreducible representation

$$\Gamma^{\mathrm{opt}} = F_{1u}. \tag{3.2}$$

The $F_{1\mathrm{u}}$-mode is polar and splits into TO and LO modes. The $F_{1\mathrm{u}}$-mode is IR active and Raman inactive [109].

Table 3.2. Raman selection rules of the optical phonon modes of crystals with wurtzite structure[a] [33]

Scattering configuration	Allowed Raman modes	Corresponding Raman tensor elements
$x(zz)x'$	A_1(TO)	α'_{zz}
$x(zy)x', x(yz)x'$	E_1(TO)	$\alpha'_{zy} = \alpha'_{yz}$
$x(yy)x'$	E_2, A_1(TO)	$\alpha'_{yy} = \pm\alpha'_{xx}$
$z(xx)z'$	E_2, A_1(LO)	$\alpha'_{xx} = \pm\alpha'_{yy}$
$z(xy)z'$	E_2	$\alpha'_{xy} = \alpha'_{yx}$

[a] It is assumed that the optical c-axis is parallel the z-direction of the laboratory system

3.2.3 Infrared Model Dielectric Function: Phonons and Plasmons

In the IR spectral region, DFs $\varepsilon_i(\omega)$ are sensitive to phonon and plasmon contributions. Hence, IR model dielectric functions (MDFs) are written as the sum of lattice $\varepsilon_i^{\mathrm{L}}(\omega)$ and free-charge-carrier $\varepsilon_i^{\mathrm{FCC}}(\omega)$ contributions [73]

$$\varepsilon_i(\omega) = \varepsilon_i^{\mathrm{L}}(\omega) + \varepsilon_i^{\mathrm{FCC}}(\omega). \tag{3.3}$$

The subscript i refers to the two polarization states parallel ($i = ||$) and perpendicular ($i = \perp$) to the c-axis, which have to be distinguished for optically uniaxial samples, for instance wurtzite-structure ZnO or sapphire. Cubic crystals, for instance rocksalt-structure $Mg_xZn_{1-x}O$, are optically isotropic and have only one DF, because the dielectric tensor is reduced to a scalar.

3.2.3.1 Lattice Contributions (Phonons)

A common way to describe $\varepsilon_i^L(\omega)$ with l lattice modes is the factorized form with Lorentzian broadening

$$\varepsilon_i^{\mathrm{L}}(\omega) = \varepsilon_{\infty,i} \prod_{j=1}^{l} \frac{\omega_{\mathrm{LO},ij}^2 - \omega^2 - i\gamma_{\mathrm{LO},ij}\omega}{\omega_{\mathrm{TO},ij}^2 - \omega^2 - i\gamma_{\mathrm{TO},ij}\omega} \,. \tag{3.4}$$

The polar lattice modes split into TO- ($\omega_{\mathrm{TO},ij}$) and LO-modes ($\omega_{\mathrm{LO},ij}$), with broadening parameters $\gamma_{\mathrm{TO},ij}$ and $\gamma_{\mathrm{LO},ij}$, respectively [73]. The parameters $\varepsilon_{\infty,i}$ denote the high-frequency limits in this model approach, which are related to the static dielectric constants $\varepsilon_{0,i}$ by the Lydanne–Sachs–Teller relation [110] (Sect. 3.3)

$$\varepsilon_{0,i} = \varepsilon_{\infty,i} \prod_{j=1}^{l} \frac{\omega_{\mathrm{LO},ij}^2}{\omega_{\mathrm{TO},ij}^2}. \tag{3.5}$$

3.2.3.2 Free-Charge-Carrier Contributions (Plasmons)

Free-charge-carrier contributions $\varepsilon_i^{\mathrm{FCC}}(\omega)$ are typically described by the classical Drude approximation

$$\varepsilon_i^{\mathrm{FCC}}(\omega) = -\frac{\omega_{\mathrm{p},i}^2}{\omega(\omega + i\gamma_{\mathrm{p},i})} \,, \tag{3.6}$$

where $\omega_{\mathrm{p},i}$ and $\gamma_{\mathrm{p},i}$ are the screened plasma frequencies and their broadening parameters, respectively. $\omega_{\mathrm{p},i}$ can be related to the free-charge-carrier concentration N and the free-charge-carrier effective mass m_i^*

$$\omega_{\mathrm{p},i}^2 = \frac{Ne^2}{\varepsilon_{\infty,i}\epsilon_0 m_i^*} \,, \tag{3.7}$$

where ϵ_0 and e denote the vacuum permittivity and the elementary charge, respectively. Assuming a constant-carrier-scattering regime, the plasma broadening parameters $\gamma_{\mathrm{p},i}$ are equal to the inverse of the energy-averaged carrier-momentum relaxation time $\langle\tau_{\mathrm{m}}\rangle_i$, and can be rewritten with the optical carrier mobility μ_i^{opt}, e, and m_i^* [111]

$$\gamma_{\mathrm{p},i} \equiv \frac{1}{\langle\tau_{\mathrm{m}}\rangle_i} = \frac{e}{m_i^* \mu_i^{\mathrm{opt}}} \,. \tag{3.8}$$

3.2.4 Visible-to-Vacuum-Ultraviolet Model Dielectric Function: Band-to-Band Transitions and their Critical-Point Structures

The DF in the visible to deep-ultraviolet (DUV) spectral region is dominated by critical point (CP) structures, which are related to electronic band-to-band transitions. For ZnO, the CP structures due to band-to-band transitions are superimposed by excitonic polarizabilities rendering the fundamental absorption edge. Within the electron-band density-of-states function, Van Hove singularities in one, two, and three dimensions occur at CPs of the type M_0–M_3 [112]. Close to energies of such singularities, band-to-band transitions occur, which give rise to the CP structures in ε. The lowest band-to-band transitions of ZnO occur at the Γ-point of the Brillouin zone, and the associated CP structures are typically of the 3DM_0 type (Sect. 3.7). At higher energies CP-structures occur, which are often described as 3DM_1-, or, equivalently, as 2DM_0- or M_2-type singularities. Different MDF approaches exist for the description of the photon energy dependence of characteristic CP structures.

In the spectral region below the electronic band-to-band transitions, the Cauchy approximation (transparency region, (3.24)) or the damped harmonic oscillator function (both transparency as well as absorption region) are often utilized as MDF approaches.

General parametric MDFs, which describe CPs and the line shape of the DF of semiconductors, are more complex. The complete MDF is the sum of multiple terms, including contributions due to 3DM_0 CP structures (ε^{3DM_0}), 2DM_0 CP structures (ε^{2DM_0}), adjacent broadened CP structures (ε^{L}), and excitonic contributions ($\varepsilon^{\mathrm{dex}}$ and $\varepsilon^{\mathrm{cex}}$). For ZnO, typically, Adachi's composite MDF is applied [76,113]. In this approach, the contributions due to 3DM_0 CP structures read

$$\varepsilon^{3DM_0}(E) = \sum_{\alpha} A_0^{\alpha} \left(E_0^{\alpha}\right)^{-3/2} \left(\frac{2 - (1+\chi_0^{\alpha})^{1/2} - (1-\chi_0^{\alpha})^{1/2}}{\left(\chi_0^{\alpha}\right)^2} \right), \tag{3.9}$$

with

$$\chi_0^{\alpha} = (E + i\Gamma_0)/E_0^{\alpha}. \tag{3.10}$$

A_0^{α} and E_0^{α} are the amplitude and the transition energy of the CP structures, respectively and Γ_0 is the broadening parameter. E is the photon energy. For wurtzite-structure and rocksalt-structure ZnO α covers $\alpha = A, B, C$ and $\alpha = D, E$, respectively. The contributions due to 2DM_0 CPs are described by

$$\varepsilon^{2DM_0}(E) = \sum_{\beta} -A^{\beta} \left(\chi^{\beta}\right)^{-2} ln(1 - \left(\chi^{\beta}\right)^2) \tag{3.11}$$

with

$$\chi^{\beta} = (E + i\Gamma^{\beta})/E^{\beta}. \tag{3.12}$$

A^{β}, E^{β}, and Γ^{β} are amplitude, transition energy, and broadening parameter, respectively. Lorentzian-broadened harmonic oscillators may be used as a good approximation for the description of adjacent (spectrally unresolvable) broadened CP structures

$$\varepsilon^{L}(E) = \sum_{\beta} \frac{A^{\beta}\Gamma^{\beta}E^{\beta}}{\left(E^{\beta}\right)^2 - E^2 - i\Gamma^{\beta}E}\ , \tag{3.13}$$

with averaged parameters A^{β}, E^{β}, and Γ^{β}. The discrete contributions (n-series) due to free excitons is approximated by [76, 113]

$$\varepsilon^{\mathrm{dex}}(E) = \sum_{\alpha} \sum_{n=1}^{\infty} \frac{A_{xb}^{n,\alpha}}{(E_0^{\alpha} - E_{xb}^{n}) - E - \mathrm{i}\Gamma_{xb}}\ . \tag{3.14}$$

$A_{xb}^{n,\alpha}$ and Γ_{xb} are amplitude and broadening parameter, respectively. E_{xb}^{n} is the free exciton binding energy of the nth excited state

$$E_{xb}^{n} = \frac{R_0^{\mathrm{3D}}}{n^2}\ . \tag{3.15}$$

R_0^{3D} is the 3D exciton Rydberg energy. At RT it is sufficient to consider $n = 1$ and, in some cases, $n = 2$. At low temperatures $n = 1, 2, 3$ might be of

interest. The exciton continuum contributions to the DF can be described by

$$\varepsilon^{\mathrm{cex}}(E) = \sum_{\alpha} \frac{A_{xc}^{\alpha} E_{xc}^{\alpha}}{4R_0^{3\mathrm{D}} \left(E + \mathrm{i}\Gamma_{xc}\right)^2} \ln \frac{\left(E_0^{\alpha}\right)^2}{\left(E_0^{\alpha}\right)^2 - \left(E + i\Gamma_{xc}\right)^2} \,, \tag{3.16}$$

with the continuum-exciton strength and broadening parameters A_{xc}^{α} and Γ_{xc}^{α}, respectively. The ground-state continuum-exciton energy E_{xc}^{α} is typically approximated by E_0^{α}.

3.2.5 Spectroscopic Ellipsometry

The main experimental technique applied in this chapter is SE. Several textbooks were written on SE [73, 114–118]. Therefore, only some basic concepts are described. SE examines the relative phase change of a polarized light beam upon reflection (or transmission) at a sample surface. In Fig. 3.4 the setup of an ellipsometry experiment is shown. Upon model analysis of the experimental data, the DFs and thicknesses of the sample constituents can be extracted. Two different experimental approaches have to be distinguished, standard and generalized ellipsometry.

3.2.5.1 Standard Spectroscopic Ellipsometry

When neither s-polarized light (light polarized perpendicular to the plane of incidence) is converted into p-polarized light (light polarized parallel to the plane of incidence) nor vice versa, standard SE is applied. This is the case for isotropic samples and for uniaxial samples in the special case, where the optical axis is parallel to the sample normal, for example (0001) ZnO [119].

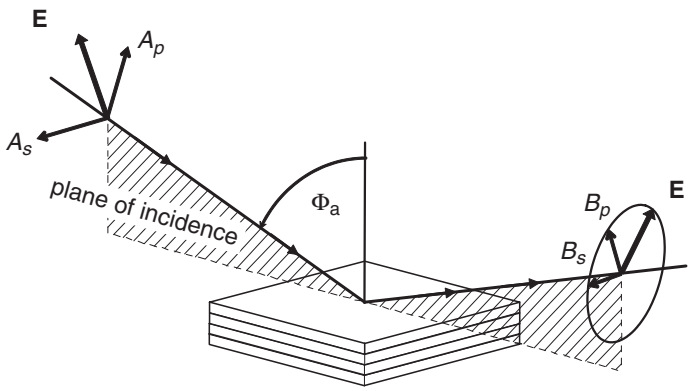

Fig. 3.4. The geometry of an ellipsometry experiment. The linearly polarized incidence light beam becomes elliptically polarized after reflection at the sample surface. The plane of incidence is shown hatched. Φ_a is the angle of incidence

Standard SE determines the complex ratio ρ of the reflection coefficients for p-polarized and s-polarized light

$$\rho = \left(\frac{B_\mathrm{p}}{A_\mathrm{p}}\right) \Big/ \left(\frac{B_\mathrm{s}}{A_\mathrm{s}}\right) = \tan\Psi \exp(\mathrm{i}\Delta)\,. \tag{3.17}$$

A_i and B_i denote the intensities of the incident and reflected light beam, respectively. Ψ and Δ are the ellipsometric parameters, where $\tan\Psi$ is the magnitude and Δ the phase of ρ [116].

3.2.5.2 Generalized Spectroscopic Ellipsometry

In the general case, when s-polarized light is converted into p-polarized light and/or vice versa, the standard SE approach is not adequate, because the off-diagonal elements of the reflection matrix $\mathbf{r}$ in the Jones matrix formalism are nonzero [114]. Generalized SE must be applied, for instance, to wurtzite-structure ZnO thin films, for which the c-axis is not parallel to the sample normal, i.e., $(11\overline{2}0)$ ZnO thin films on $(1\overline{1}02)$ sapphire [43, 71]. Choosing a Cartesian coordinate system relative to the incident (A_i) and reflected plane waves (B_i), as shown in Fig. 3.4, the change of polarization upon reflection can be described by [117, 120]

$$\begin{pmatrix} B_\mathrm{p} \\ B_\mathrm{s} \end{pmatrix} = \mathbf{r} \begin{pmatrix} A_\mathrm{p} \\ A_\mathrm{s} \end{pmatrix} = \begin{pmatrix} r_\mathrm{pp} & r_\mathrm{sp} \\ r_\mathrm{ps} & r_\mathrm{ss} \end{pmatrix} \begin{pmatrix} A_\mathrm{p} \\ A_\mathrm{s} \end{pmatrix} . \tag{3.18}$$

The generalized ellipsometric parameters Ψ_{ij} and Δ_{ij} are defined by

$$\frac{r_\mathrm{pp}}{r_\mathrm{ss}} \equiv R_\mathrm{pp} = \tan\Psi_\mathrm{pp} \exp(\mathrm{i}\Delta_\mathrm{pp})\ , \tag{3.19}$$

$$\frac{r_\mathrm{ps}}{r_\mathrm{pp}} \equiv R_\mathrm{ps} = \tan\Psi_\mathrm{ps} \exp(\mathrm{i}\Delta_\mathrm{ps})\ , \tag{3.20}$$

$$\frac{r_\mathrm{sp}}{r_\mathrm{ss}} \equiv R_\mathrm{sp} = \tan\Psi_\mathrm{sp} \exp(\mathrm{i}\Delta_\mathrm{sp})\ . \tag{3.21}$$

3.2.5.3 Data Analysis

Only in the special case of isotropic bulk samples, the experimental data can be transformed directly into the sample's DF. In all other cases a model analysis is required, where the layered sample structure has to be considered appropriately, i.e., the DFs, thickness, and, in case of anisotropic materials, the crystal orientation of each single layer. Unknown parameters are varied until experimental and model data match as close as possible. Upon the use of parameterized MDFs, physically relevant parameters of the samples can be obtained. Typical MDFs for ZnO are described in Sects. 3.2.3 and 3.2.4.

3.3 Dielectric Constants and Dielectric Functions

Figure 3.5 summarizes typical DF spectra $\varepsilon = \varepsilon_1 + i\varepsilon_2$ of ZnO. The DF spectra were obtained by SE in the Mid-IR (MIR), Near-IR (NIR), visible (VIS), ultraviolet (UV), and vacuum-ultraviolet (VUV) spectral region from both single-crystal bulk and thin film samples. DF spectra of ZnO in the NIR–VIS–UV spectral region were also reported in [76, 78, 80–82, 121, 122], and for $Mg_xZn_{1-x}O$ in [82, 90]. Phonon-mode contributions (Sect. 3.4), plasmon-mode (free-charge-carrier) contributions (Sect. 3.5), refractive indices (Sect. 3.6), critical-point and electronic band-to-band transition parameters as well as their excitonic contributions (Sect. 3.7) can be obtained from the DF spectra, including their anisotropy. While the DFs of ZnO in the IR exhibit appreciable anisotropy, in the below-band-gap spectral region and above the band gap, $\varepsilon_\perp$ and $\varepsilon_\parallel$ show only small differences. ZnO is uniaxial positive, i.e., $Re\{\varepsilon_{||}\} > Re\{\varepsilon_\perp\}$, at frequencies below and above the reststrahlen band [123], and throughout the entire band-gap region [77, 124].

The static dielectric constants $\varepsilon_{0,i}$ can be determined from the analysis of IR spectra with sufficient spectral data coverage below and above the reststrahlen regions. For photon energies far above the phonon resonances but still sufficiently below the electronic band-to-band transitions, the DFs converge to the "high-frequency" dielectric constants $\varepsilon_{\infty,i}$, which is related to $\varepsilon_{0,i}$ by the Lyddane–Sachs–Teller relation (3.5). $\varepsilon_{\infty,i}$ measure the sum of

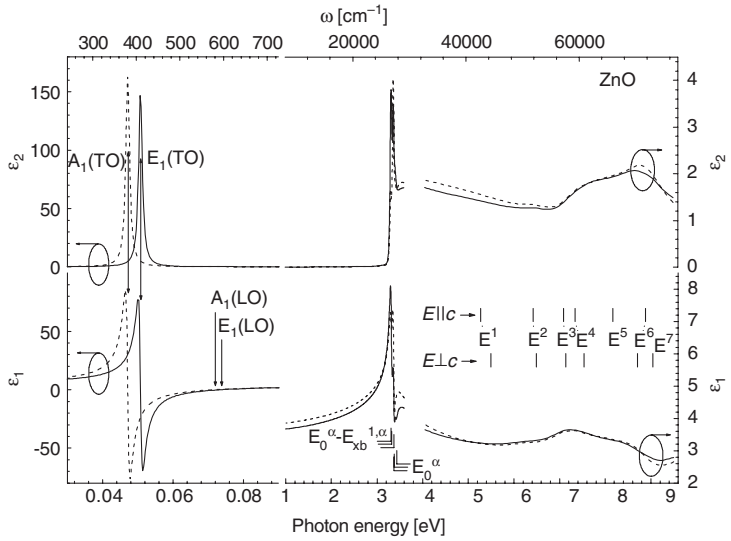

Fig. 3.5. Real (ε_1) and imaginary part (ε_2) of the DFs $\varepsilon = \varepsilon_1 + i\varepsilon_2$ of ZnO at RT for polarization perpendicular (*solid lines*) and parallel (*dashed lines*) to the *c*-axis determined by SE [15, 38, 71, 91]. Optical phonon modes (Table 3.4; Sect. 3.4) and transition energies (Tables 3.9, 3.10; Sect. 3.7) are marked. Note the different scales for the IR-to-NIR and the VIS-to-VUV spectral regions

all linear electronic polarizabilities for all photon energies within and above the fundamental band-to-band transition energy until the shortest end of the electromagnetic spectrum. Table 3.3 summarizes "high-frequency" and static dielectric constants of ZnO. The dielectric constants for the ZnO thin films are smaller than those of the ZnO bulk samples, which can be explained by the lower film density relative to that of the bulk samples, or because of slightly different compositions.

Figure 3.6 summarizes "high-frequency" and static dielectric constants of PLD-grown $Mg_xZn_{1-x}O$ thin films [43, 62, 72, 74]. Besides the natural

Table 3.3. "High-frequency" $\varepsilon_{\infty,i}$ and static $\varepsilon_{0,i}$ dielectric constants of ZnO bulk samples (b) and ZnO thin films (f)

Ref.		Method		$\varepsilon_{\infty,\perp}$	$\varepsilon_{\infty,\|\|}$	$\varepsilon_{0,\perp}$	$\varepsilon_{0,\|\|}$
Bond (1965)	[124]	NIR-VIS minimum deviation	(b)	3.70	3.75	7.78	8.74
Yoshikawa (1997)	[76]	NIR-VIS SE	(b)	3.68	3.72	7.74	8.67
Teng (2000)	[95]	NIR-VIS prism coupling	(f)[b]	3.60	3.66	7.44	8.45
Ashkenov (2003)	[38]	IRSE	(b)	3.70	3.78	7.78	8.81
Ashkenov (2003)	[38]	IRSE	(f)[b]	3.61	3.76	7.46	8.69
Bundesmann (2004)	[71]	IRSE	(f)[c]	3.53	3.60	7.29	8.37
Bundesmann (2006)	[43]	IRSE	(f)[d]	3.67†		7.96†	
Bundesmann (2006)	[43]	IRSE	(f)[e]	3.38†		6.82†	
Bundesmann (2006)	[43]	IRSE	(f)[f]	2.99†		6.03†	

[a] $\varepsilon_{\infty,i}$ follows from $\varepsilon_{0,i}$ with the Lydanne–Sachs–Teller-relation (3.5) and the phonon-mode frequencies in Table 3.4
[b] (0001) ZnO film (PLD) on (0001) sapphire
[c] $(11\bar{2}0)$ ZnO film (PLD) on $(1\bar{1}02)$ sapphire
[d] (0001) ZnO film (PLD) on (001) silicon
[e] ZnO film (magnetron sputtering) on metallized foil
[f] ZnO film (magnetron sputtering) on metallized glass
† Isotropically averaged

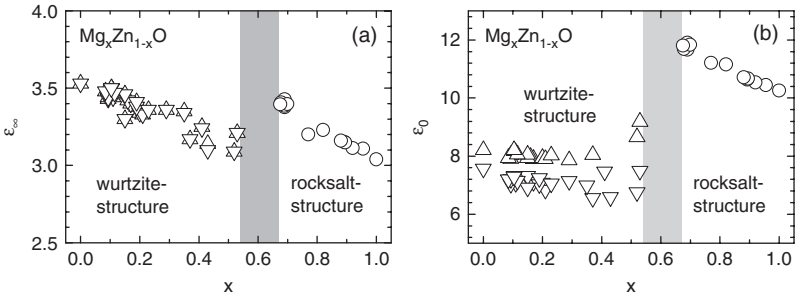

Fig. 3.6. "High-frequency" dielectric constants (**a**) and static dielectric constants (**b**) of wurtzite-structure ($E||c$: *up-triangles*, $E\perp c$: *down-triangles*) and rocksalt-structure (*circles*) $Mg_xZn_{1-x}O$ thin films [43, 62, 72, 74]. The *shaded area* indicates the composition range of the phase transition. Reprinted with permission from [74]

disappearance of the anisotropy both "high-frequency" and static dielectric constants change abruptly upon the phase transition from wurtzite to rocksalt structure because of the coordination number change (4–6) and the associated change of bond polarizability (increase in splitting between TO and LO phonon-mode frequencies, Fig. 3.13, Sect. 3.4.3), and critical-point characteristics of the two polytypes (Sect. 3.7.2).

3.4 Phonons

3.4.1 Undoped ZnO

Table 3.4 summarizes the phonon-mode frequencies of ZnO bulk samples and ZnO thin films, as obtained by Raman scattering spectroscopy, IR-reflection measurements, and IRSE.

Figure 3.7 presents typical Raman spectra of a ZnO bulk sample and a ZnO thin film on sapphire. According to the theoretical considerations in Sect. 3.2.2, the scattering intensities at $\omega \sim 379\,\mathrm{cm}^{-1}$, $\sim 410\,\mathrm{cm}^{-1}$, $\sim 437\,\mathrm{cm}^{-1}$, and $\sim 572\,\mathrm{cm}^{-1}$ can be assigned to the A_1(TO)-, E_1(TO)-, $E_2^{(2)}$-, and A_1(LO)-mode, respectively. The scattering cross-section of the A_1(LO)-mode is markedly smaller than that of the A_1(TO)-mode, which was explained by the destructive interference of the Fröhlich interaction and the deformation potential contributions to the LO-scattering in ZnO [31]. The intensities at $\omega \sim 332$, ~ 538, and $\sim 665\,\mathrm{cm}^{-1}$ were assigned to multiple-phonon scattering processes [32, 35], whereas the spectral feature at $\omega \sim 589\,\mathrm{cm}^{-1}$ was assigned to the E_1(LO)-mode. The phonon modes of the ZnO thin film occur at similar frequencies as those of the ZnO bulk sample, but the Raman spectra contain additional spectral features because of the sapphire substrate [125, 126].

In Fig. 3.8, typical IRSE spectra of a ZnO bulk sample and a ZnO film on sapphire are plotted. In the Ψ-spectrum of the ZnO bulk sample a plateau with $\Psi \sim 45°$ can be seen, which corresponds to the bands of total reflection (reststrahlen bands), which occurs between the E_1(TO)- and E_1(LO)-mode frequencies [123]. The small dip within the plateau is caused by the loss in p-reflectivity, and localizes the A_1(LO)- and E_1(LO)-mode frequencies. The derivative-like structure in the Ψ-spectrum of the bulk ZnO sample at $\omega \sim 650\,\mathrm{cm}^{-1}$ is caused by the anisotropy $\mathrm{Re}\{\varepsilon_{||}\} > \mathrm{Re}\{\varepsilon_{\perp}\}$ (Sect. 3.3) [38].

In the Ψ-spectrum of the ZnO thin film, a similar plateau as in the Ψ-spectrum of the ZnO bulk sample is present. However, the phonon modes of the sapphire substrate introduce additional features, for example at $\omega \sim 510$, ~ 630, and $\sim 900\,\mathrm{cm}^{-1}$ [38,123]. The spectral feature at $\omega \sim 610\,\mathrm{cm}^{-1}$ is called the Berreman resonance, which is related to the excitation of surface polaritons of transverse magnetic character at the boundary of two media [73]. In the spectral region of the Berreman resonance, IRSE provides high sensitivity to the A_1(LO)-mode parameters. For (0001)-oriented surfaces of crystals with wurtzite structure, linear-polarization-dependent spectroscopic

Table 3.4. Frequencies of long-wavelength optical phonon modes of ZnO bulk samples (b) and ZnO thin films (f)[a]

Ref.	Method		$E_2^{(1)}$	A_1(TO)	E_1(TO)	$E_2^{(2)}$	A_1(LO)	E_1(LO)
Collins (1959)	[63] IR-refl.	(b)	–	–	414	–	–	591
Heltemes (1967)	[64] IR-refl.	(b)	–	377	406	–	575	589
Venger (1995)	[65] IR-refl.	(b)	–	380	412	–	570	591
Damen (1966)	[32] Raman	(b)	101	380	407	437	–	583
Arguello (1969)	[33] Raman	(b)	101	380	413	444	579	591
Scott (1970)	[34] Raman	(b)	–	–	–	–	574	583
Callender (1973)	[31] Raman	(b)	–	381	407	441	–	583
Calleja (1977)	[35] Raman	(b)	98	378.5	410	438	–	590
Bairamov (1983)	[36] Raman	(b)	98	378	409.5	437.5	576	588
Decremps (2001)	[37] Raman	(b)	99	382	414	439	574	580
Ashkenov (2003)	[38] Raman	(b)	–	378	409	437	572	588
Lu (2000)	[39] Raman	(f)[b,c]	–	–	–	438	–	579
Zeng (2002)	[40] Raman	(f)[c]	–	–	–	437	–	579
Ashkenov (2003)	[38] Raman	(f)[b]	–	378	410	437	–	588
Ye (2003)	[41] Raman	(f)[d]	–	–	–	436	563	–
Bundesmann (2006)	[43] Raman	(f)[c]	–	376	410	437	–	–
Ashkenov (2003)	[38] IRSE	(b)	–	–	408.2	–	577.1	592.1
Ashkenov (2003)	[38] IRSE	(f)[b]	–	–	409.1	–	574.5	588.3
Bundesmann (2004)	[71] IRSE	(f)[e]	–	376.5	410.7	–	574.1	590.4
Heitsch (2005)	[30] IRSE	(f)[c]	–	–	406.0	–	571.3	–
Bundesmann (2006)	[43] IRSE	(f)[f]	–		406.2[†]	–	577.0[†]	
Bundesmann (2006)	[43] IRSE	(f)[g]	–		409.9[†]	–	581.9[†]	
Decremps (2001)	[37] Theory		92	397	426	449	559	577

[a] All values are given in units of cm^{-1}
[b] (0001) ZnO film (PLD) on (0001) sapphire
[c] (0001) ZnO film (PLD) on (001) silicon
[d] (0001) ZnO film (MOCVD) on (111) silicon
[e] $(11\bar{2}0)$ ZnO film (PLD) on $(1\bar{1}02)$ sapphire
[f] ZnO film (magnetron sputtering) on metallized foil
[g] ZnO film (magnetron sputtering) on metallized glass
[†] Isotropically averaged

techniques, as for instance IRSE, are not sensitive to the A_1(TO)-mode, and are only slightly sensitive to the E_1(LO)-mode. This limitation can be overcome by application of generalized IRSE to optically uniaxial thin films, which are not (0001)-oriented [43, 71, 73]. Figure 3.9 shows the generalized IRSE data (Ψ_{ij} only) of a $(11\bar{2}0)$ ZnO thin film on $(1\bar{1}02)$ sapphire, which allows to extract simultaneously the complete DF spectra for $\varepsilon_{||}$ and $\varepsilon_{\perp}$ (Fig. 3.5), the crystal orientation for both the ZnO thin film and the sapphire substrate, and the thin film thickness. Typical IRSE spectra of a PLD-grown ZnO thin film on silicon and two magnetron-sputtered ZnO thin films on metallized foil or glass are shown in Fig. 3.10. The corresponding

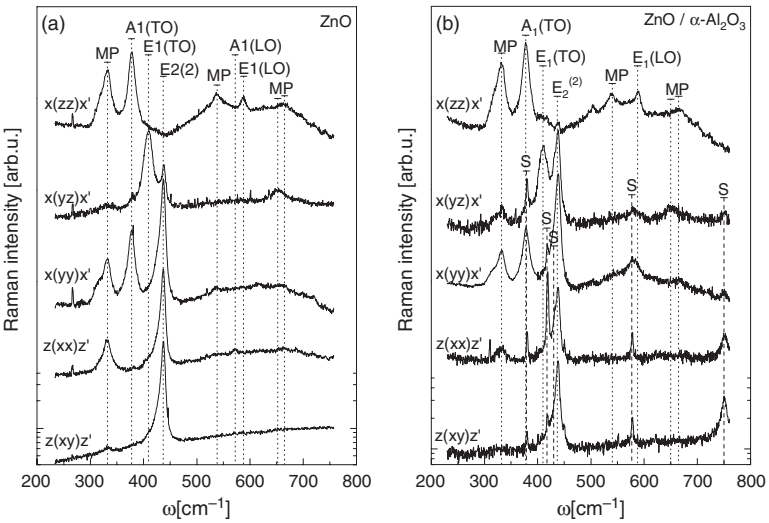

Fig. 3.7. Polarized micro-Raman spectra of a (0001) ZnO bulk sample (**a**) and a (0001) ZnO thin film ($d \sim 1,970$ nm) on (0001) sapphire (**b**). The vertical *dotted* and *dashed lines* mark ZnO and sapphire (S) phonon modes, respectively. MP denotes modes due to multi-phonon scattering processes in ZnO. Excitation with Ar^+-laser line $\lambda = 514.5$ nm and laser power $P \leq 40$ mW. Reprinted with permission from [38]

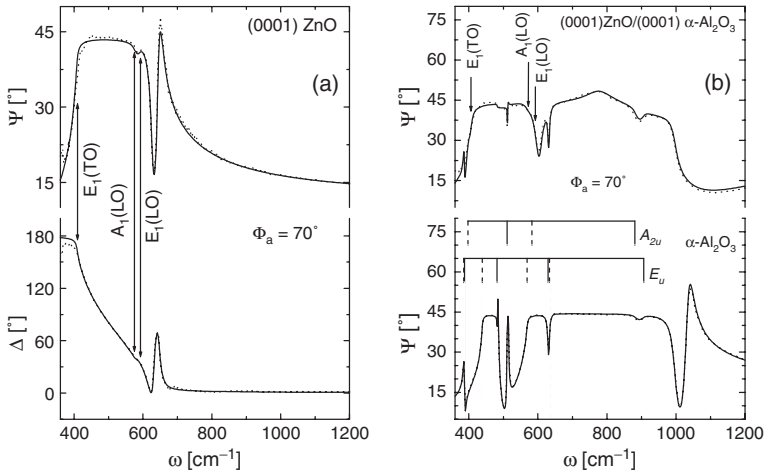

Fig. 3.8. (**a**) Experimental (*dotted lines*) and best-fit model (*solid lines*) IRSE spectra of a (0001) ZnO bulk sample. The ZnO phonon modes, as obtained by IRSE, are marked by *vertical arrows*. (**b**) Experimental (*dotted lines*) and best-fit model (*solid lines*) IRSE spectra (Ψ only) of a (0001) ZnO thin film on (0001) sapphire (*upper panel*, thickness $d \sim 1\,970$ nm) and of a bare (0001) sapphire substrate (*lower panel*). The ZnO phonon modes, as obtained by IRSE, are marked by *arrows*. The IR-active modes of sapphire are indicated by *solid* (TO) and *dotted* (LO) *vertical markers*. Reprinted with permission from [38]

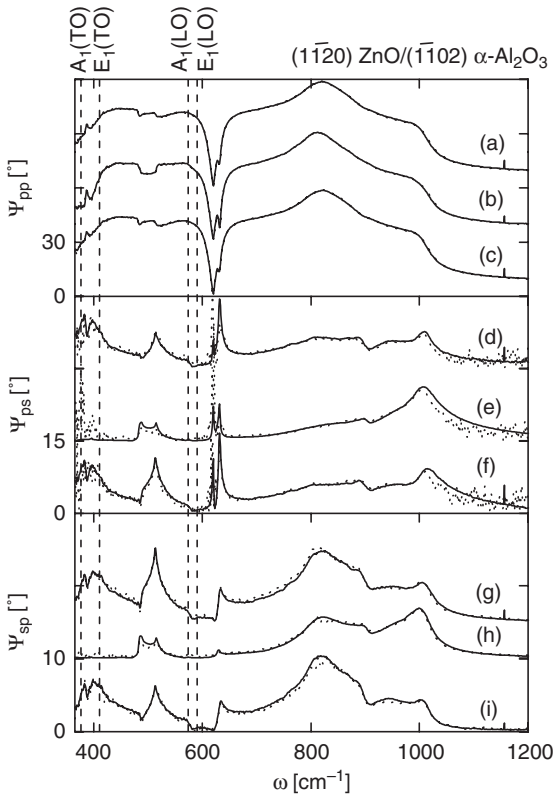

Fig. 3.9. Experimental (*dotted lines*) and best-model (*solid lines*) generalized IRSE spectra Ψ_{ij} of a (11$\bar{2}$0) ZnO thin film ($d = 1455 \pm 5$ nm) on (1$\bar{1}$02) sapphire [43,71]. Spectra are shifted for clarity. *Vertical dashed lines* indicate the ZnO phonon mode frequencies. Spectra in (a,d,g), (b,e,h), and (c,f,i) belong to different sample azimuth angles, respectively. The best-model values of the Euler angle θ_{ZnO}, $\theta_{\mathrm{Sapphire}}$, which describe the *c*-axis inclination with respect to the sample normal are $89.0° \pm 1.0°$ and $54.9° \pm 0.8°$, respectively. Reprinted with permission from [71]

phonon-mode frequencies are listed in Table 3.4. Because of the submicrometersized randomly-oriented polycrystalline structure of the magnetron-sputtered ZnO thin films, the optical response is isotropic, and the MDF is that for an isotropic film providing phonon-mode parameters intermediate to those of A_1- and E_1-modes of a single-crystalline ZnO thin film.

Temperature-dependent Raman data were reported for the $E_2^{(2)}$-mode of flux-grown ZnO platelets in the temperature range from $T \sim 15\,\mathrm{K}$ to $T \sim 1\,050\,\mathrm{K}$ [127], and for the $E_2^{(1)}$-mode, the $E_2^{(2)}$-mode, and the MP-mode at $\omega \sim 332\,\mathrm{cm}^{-1}$ of a ZnO bulk sample in the temperature range from $T \sim 300\,\mathrm{K}$ to $T \sim 700\,\mathrm{K}$ [43] In Fig. 3.11 the unpolarized Raman spectra and the temperature-dependence of the phonon-mode frequencies from [43] are

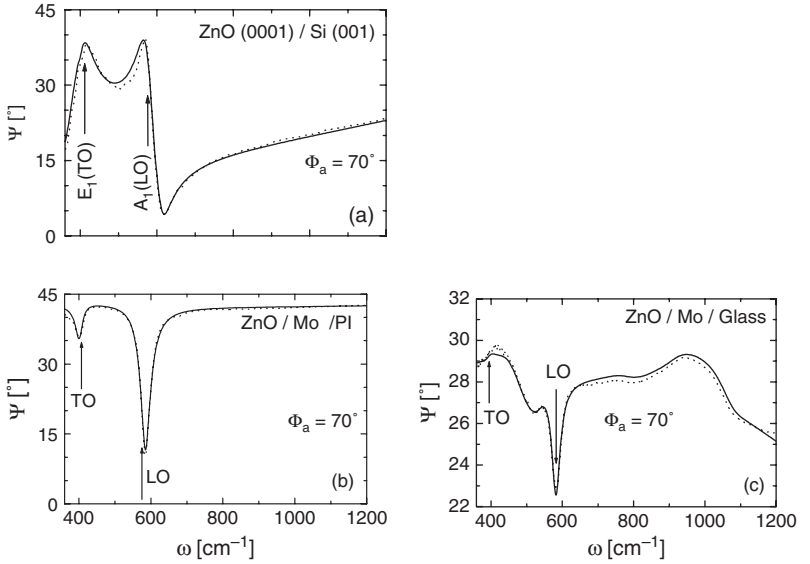

Fig. 3.10. Experimental (*dotted lines*) and best-fit model (*solid lines*) IRSE spectra of a PLD-grown (0001) ZnO thin film on (001) silicon (*panel (a)*, film thickness $d \sim 670\,\mathrm{nm}$), and magnetron-sputtered ZnO thin films on metallized polyimide foil (*panel (b)*, $d \sim 500\,\mathrm{nm}$) and on metallized glass (*panel (c)*, $d \sim 30\,\mathrm{nm}$) [43]. ZnO phonon-mode frequencies, as obtained by best-model analysis, are marked by *vertical arrows*

plotted. The temperature-dependence can be modeled by the empirical Bose–Einstein equation [128, 129]

$$\omega(T) = \omega(0) - \frac{A}{\exp[B\hbar\omega(0)/k_\mathrm{B}T] - 1}\,. \tag{3.22}$$

A and B are model parameters representing the high-temperature linear slope ($\partial\omega/\partial T|_{T\to\infty}$) and effective phonon-mode temperature ($B\hbar\omega(0)/k_\mathrm{B}$), respectively. $\omega(0)$ is the phonon-mode frequency at $T = 0\,\mathrm{K}$. Table 3.5 summarizes the best-model parameters reported in [43]. In [127], a linear temperature-dependence with $\partial\omega[E_2^{(2)}]/\partial T = -1.85 \times 10^{-2}\mathrm{cm}^{-1}\mathrm{K}^{-1}$ was reported for temperatures above RT.

The pressure-dependence of ZnO phonon-mode frequencies measured by Raman scattering was reported in [37, 130]. From that the Grüneisen parameters γ_j

$$\gamma_j = -\frac{\partial \ln \omega_j}{\partial \ln V} \tag{3.23}$$

of the vibrational modes can be obtained. Table 3.6 summarizes the Grüneisen parameters reported in [37].

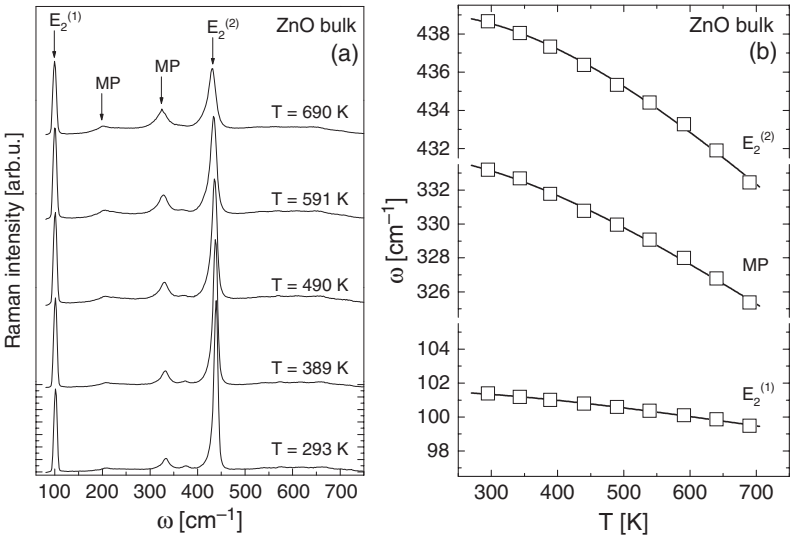

Fig. 3.11. (**a**) Temperature-dependent, unpolarized Raman spectra of a (0001) ZnO bulk sample [43]. Spectra are shifted for clarity. (**b**) Phonon-mode frequencies vs. temperature as determined from the Raman data in Fig. 3.11a. The *solid lines* are model approximations according to (3.22). Excitation with Nd:YAG-laser line $\lambda = 532\,\mathrm{nm}$ and laser power $P \sim 60\,\mathrm{mW}$

Table 3.5. Best-model parameters of the temperature-dependent phonon mode shift in Fig. 3.11b, calculated by (3.22) (Bose–Einstein model) [43]

Mode	$\omega(0)$ (cm^{-1})	A (cm^{-1})	$B\hbar\omega(0)/k_\mathrm{B}$ (K)	$\partial\omega/\partial T\|_{T\to\infty}$ ($\mathrm{cm}^{-1}\mathrm{K}^{-1}$)
$E_2^{(1)}$	101.6 ± 0.1	6.7 ± 1.7	$1\,000 \pm 150$	-0.007 ± 0.002
MP	334.1 ± 0.4	29.3 ± 6.6	$1\,020 \pm 140$	-0.03 ± 0.01
$E_2^{(2)}$	439.2 ± 0.3	48 ± 9	$1\,290 \pm 120$	-0.037 ± 0.01

Table 3.6. Grüneisen parameters of the zone-center phonon modes of ZnO [37]

Mode j	Experiment γ_j	Theory γ_j
$E_2^{(1)}$	–1.6	–1.67
A_1(TO)	2.1	1.70
E_1(TO)	1.8	1.80
$E_2^{(2)}$	2.0	1.84
E_1(LO)	1.4	1.30

3.4.2 Doped ZnO

Figure 3.12 shows typical Raman spectra of several doped ZnO thin films. Additional modes (AM), occurring at $\omega \sim 275$, ~ 510, ~ 582, ~ 643, and $\sim 856\,\mathrm{cm}^{-1}$ (the first four of them are shown and marked by vertical solid lines in Fig. 3.12), were first assigned to N-incorporation [49–51], because the intensity of these modes was reported to increase with increasing N-content [50]. However, the AMs appear also in Raman spectra of ZnO samples doped with other elements (Fig. 3.12a), [48,52,53]). Therefore, it was suggested that the AMs are related to defect-induced modes [48]. Theoretical considerations confirmed this assignment [131]. It was discussed that the AMs could be related to modes of ZnO, which are Raman-inactive within a perfect crystal. Upon doping-induced defect formation, the translational crystal symmetry can be broken, and Raman-inactive modes may become Raman-active. The Raman spectra of the ZnO thin films with transition metals in Fig. 3.12b show a different behavior than those in Fig. 3.12a [43, 48]. Raman spectra of $Fe_{0.08}Zn_{0.92}O$ contain the above described AMs, but with different intensity ratios. For MnZnO, CoZnO, and NiZnO a broad band between $\omega \sim 500\,\mathrm{cm}^{-1}$

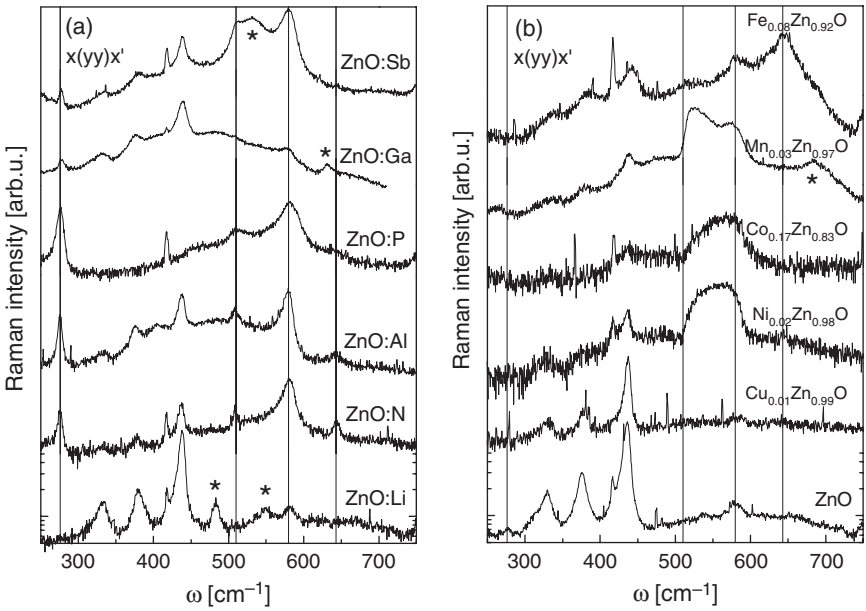

Fig. 3.12. Micro-Raman spectra in the $x(yy)x'$ scattering configuration of several PLD-grown, element-doped wurtzite-structure (0001) ZnO thin films on (0001) sapphire [43,48]. Defect-induced modes are marked by *solid vertical lines*. The *asterisks* indicate modes, which seem to occur for specific dopant species only. Excitation with Ar^+-laser line $\lambda = 514.5\,\mathrm{nm}$ and laser power $P \leq 40\,\mathrm{mW}$

and $\omega \sim 600\,\mathrm{cm}^{-1}$ occurred [43, 58], which was also assigned to defects. Additionally, some AMs appear to be characteristic for their dopant species (Fig. 3.12).

3.4.3 $Mg_xZn_{1-x}O$

The phonon mode frequencies of wurtzite- and rocksalt-structure $Mg_xZn_{1-x}O$ thin films vs. x, as obtained by combination of Raman scattering and IRSE, are plotted for $0 \leq x \leq 1$ in Fig. 3.13.

For the wurtzite-structure $Mg_xZn_{1-x}O$ ($x \leq 0.53$) thin films, an one-mode behavior with a further weak mode between the TO- and LO-mode for the phonons with E_1- and A_1-symmetry was found. The A_1(TO)-, A_1(LO)-, and the upper branch of the E_1(LO)-modes of the wurtzite-structure thin films show an almost linear behavior, whereas the lower branch of the E_1(LO)-modes and the two E_1(TO)-branches exhibit a nonlinear behavior. In [132] the modified random element isodisplacement (MREI) model was suggested

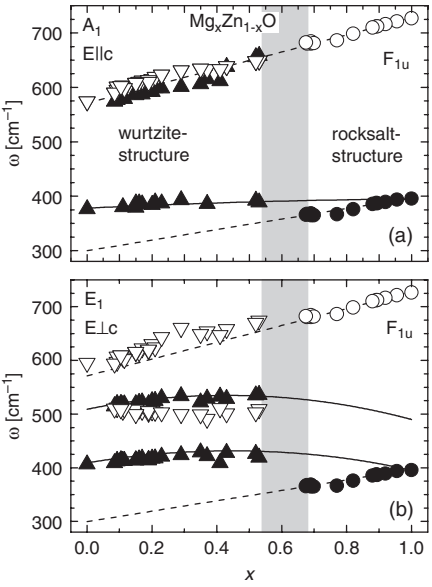

Fig. 3.13. Phonon-mode frequencies of wurtzite-structure PLD-grown $Mg_xZn_{1-x}O$ thin films with A_1-symmetry (**panel a**, *triangles*) and E_1-symmetry (**panel b**, *triangles*), and of rocksalt-structure PLD-grown $Mg_xZn_{1-x}O$ thin films (*circles* in both panels) vs. x [43, 62, 72, 74]. *Open* and *solid symbols* represent TO- and LO-modes, respectively. The *dashed lines* are linear approximations of the rocksalt-structure phonon modes from [74], the *solid lines* represent MREI calculations for the wurtzite-structure phonon modes redrawn from [132]. The *shaded area* marks the composition range, where the phase transition occurs. Reprinted with permission from [74]

to describe the phonon-mode behavior vs. x. A good agreement for the E_1(TO)-, A_1(TO)-, and A_1(LO)-branches was obtained. The AM of the upper TO-branch with E_1-symmetry was assigned to the mixed mode of the $Mg_xZn_{1-x}O$ alloy, which originates from the local mode $\omega_{\mathrm{loc,ZnO:Mg}}$ of Mg in ZnO. The extrapolation to $x = 0$ yields an experimental value of $\omega_{\mathrm{loc,ZnO:Mg}} = 509\,\mathrm{cm}^{-1}$. This value agrees well with the calculated local mode $\omega_{\mathrm{loc,ZnO:Mg}} = 518\,\mathrm{cm}^{-1}$ [43, 74].

For rocksalt-structure $Mg_xZn_{1-x}O$ thin films ($x \geq 0.68$), an one-mode behavior was found by IRSE, where both the TO- and LO-modes shift linearly with x. The phonon-mode frequencies of the MgO thin film agree well with values of MgO single crystals ($\omega_{\mathrm{TO}} = 401\,\mathrm{cm}^{-1}$, $\omega_{\mathrm{LO}} = 719\,\mathrm{cm}^{-1}$ [133]). The shift of the TO- and LO-modes can be modeled by a linear composition-dependence $\omega_{\mathrm{TO;LO}}(x) = m_{\mathrm{TO;LO}}x + n_{\mathrm{TO;LO}}$ with best-fit coefficients $m_{\mathrm{TO}} = 97 \pm 4\,\mathrm{cm}^{-1}$, $n_{\mathrm{TO}} = 300 \pm 3\,\mathrm{cm}^{-1}$, $m_{\mathrm{LO}} = 157 \pm 10\,\mathrm{cm}^{-1}$, and $n_{\mathrm{LO}} = 571 \pm 9\,\mathrm{cm}^{-1}$ [43]. The extrapolation to $x = 0$ yield a value of $\omega_{\mathrm{TO}}(0) \sim 300\,\mathrm{cm}^{-1}$ and $\omega_{\mathrm{LO}}(0) \sim 570\,\mathrm{cm}^{-1}$, which should address ω_{TO} and ω_{LO}, respectively, of rocksalt-structure ZnO. No experimental data have been reported for rocksalt-structure ZnO at normal ambient conditions yet. In [134], ab initio calculations for phonon properties of rocksalt-structure ZnO were presented, which used experimental data of rocksalt-structure ZnO studied at high pressures (∼8 GPa) as input parameters. According to these calculations, ω_{TO} and ω_{LO} of rocksalt-structure ZnO were predicted to be 235 and $528\,\mathrm{cm}^{-1}$, respectively. The values are smaller than those obtained from the IRSE analysis described earlier, but both extrapolations follow the same trend in predicting phonon-mode frequencies, which are smaller than those of wurtzite-structure ZnO.

3.4.4 Phonon Mode Broadening Parameters

The phonon mode broadening parameter of the ZnO bulk sample[2] in Fig. 3.8a is $\gamma_\perp = 13 \pm 1\,\mathrm{cm}^{-1}$. Similar values were reported for the (0001) ZnO thin film on (0001) sapphire in Fig. 3.8b: $\gamma_\perp = 10 \pm 1\,\mathrm{cm}^{-1}$, and the $(11\bar{2}0)$ ZnO thin film on *a*-plane sapphire in Fig. 3.9: $\gamma_{||} = 15.1 \pm 0.2\,\mathrm{cm}^{-1}$, $\gamma_\perp = 10.7 \pm 0.5\,\mathrm{cm}^{-1}$.[3] Accordingly, the crystal quality of these ZnO thin films are comparable with that of the ZnO bulk sample, which was confirmed by X-ray diffraction [43].

Typical phonon mode broadening parameters for a set of ZnO thin films grown on silicon by PLD with varying oxygen partial pressure and/or substrate heater power are shown in Fig. 3.14. Heitsch et al. [30] observed that the

[2] For (0001)-oriented ZnO films, IRSE data are not sensitive to the A_1(TO) mode. Accordingly, the broadening parameter $\gamma_{||}$ cannot be determined. For setting up the MDF parameters, it is then often assumed $\gamma_{||} = \gamma_\perp$, which has no influence on the validity of $\gamma_\perp$ [73].

[3] For off-axis oriented ZnO samples, both $\gamma_{||}$ and $\gamma_\perp$ can be determined [73]

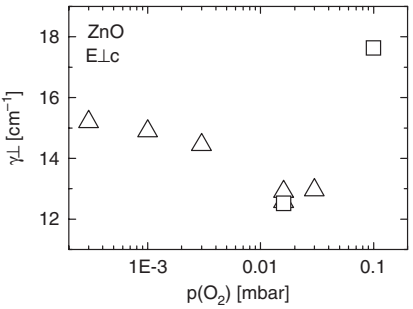

Fig. 3.14. Phonon mode broadening parameters, as determined by IRSE, vs. oxygen partial pressure for a set of PLD-grown ZnO thin films on (111) silicon. *Triangles* and *squares* represent data of thin films grown with substrate heater power of $P = 400\,\mathrm{W}$ and $P = 600\,\mathrm{W}$, respectively. Reprinted with permission from [30]

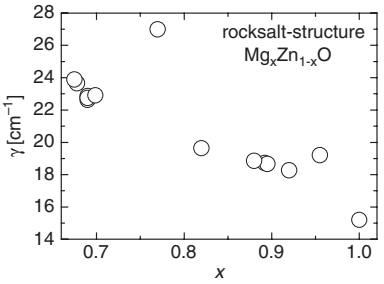

Fig. 3.15. Phonon mode broadening parameters of PLD-grown rocksalt-structure $Mg_xZn_{1-x}O$ thin films on sapphire. Reprinted with permission from [74]

phonon-mode frequencies vary only slightly, but the phonon mode broadening parameters showed a systematic variation with varying $p(O_2)$. This variation is assigned to a varying crystal quality, which was confirmed by TEM and PL measurements [30]. The crystal quality is suggested to be best, when the oxygen partial pressure is chosen between $p(O_2) = 0.01\,\mathrm{mbar}$ and $p(O_2) = 0.03\,\mathrm{mbar}$. Too much or too few oxygen seems to introduce more defects.

The broadening parameters are also influenced by the growth technique, the substrate material, and the film thickness. For example, as can be seen from the IRSE spectra of the ZnO thin films in Fig. 3.10a (PLD, silicon substrate, $d \sim 670\,\mathrm{nm}$), b (magnetron sputtering, metallized foil, $d \sim 500\,\mathrm{nm}$), c (magnetron sputtering, metallized glass, $d \sim 30\,\mathrm{nm}$),[4] where $\gamma_\perp = 14 \pm 1\,\mathrm{cm}^{-1}$, $\gamma = 23 \pm 1\,\mathrm{cm}^{-1}$, and $\gamma = 32 \pm 1\,\mathrm{cm}^{-1}$ was found, respectively, indicating a decreasing crystal quality from (a) to (c).

In addition to defects and impurity incorporation, alloy-induced disorder further increases the phonon mode broadening parameters, as discussed

[4] Magnetron-sputtered films contain randomly oriented crystallites, and the optical response is isotropic with one lattice mode broadening parameter only.

in [43,72,74] for rocksalt-structure $Mg_xZn_{1-x}O$ thin films (Fig. 3.15). Except for the data point with $x = 0.78$, a systematic increment of γ with increasing Zn-content is obvious.[5]

3.5 Plasmons

So far, all observed free-charge-carrier contributions to the optical properties of ZnO and related materials are only due to n-type conductivity, because reproducible and sufficiently high p-type conductivity is still a challenge. Therefore, all data presented here address n-type conductive samples.

Figures 3.16 and 3.17 depict typical IRSE spectra of PLD-grown ZnO thin films doped with different Ga- and Al-contents, respectively, reflecting the influence of the free charge carriers on the IR response of the doped ZnO thin films [43].

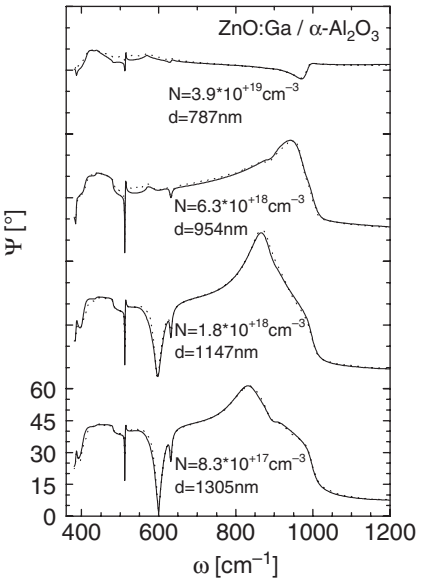

Fig. 3.16. Experimental (*dotted lines*) and best-model calculated (*solid lines*) IRSE spectra of PLD-grown Ga-doped ZnO thin films on sapphire with different free-charge-carrier concentration and thickness parameters as indicated next to the respective graphs [43]. Spectra are shifted for clarity

[5] The $Mg_{0.78}Zn_{0.22}O$ thin film was grown at a higher oxygen partial pressure ($p(O_2) = 0.16$ mbar) than all other films ($p(O_2) = 0.01 \ldots 0.05$ mbar). Therefore, γ is not only increased by the alloying-effect, but also by a lower crystal quality (see Fig. 3.14).

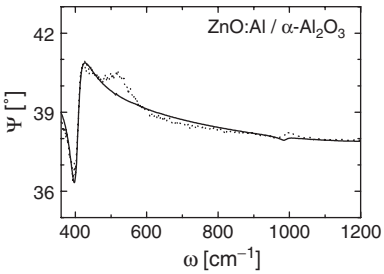

Fig. 3.17. Experimental (*dotted lines*) and best-model (*solid lines*) IRSE spectra of an highly Al-doped ZnO thin film ($d \sim 1\,400$ nm) grown by PLD on sapphire [43]. The best-model free-charge-carrier parameters are $N = (5.7 \pm 0.1) \times 10^{19}\,\mathrm{cm}^{-3}$, $\mu_{||}^{\mathrm{opt}} = 7\,\mathrm{cm}^2\,\mathrm{Vs}^{-1}$, and $\mu_{\perp}^{\mathrm{opt}} = 106\,\mathrm{cm}^2\,\mathrm{V}^{-1}\,\mathrm{s}^{-1}$

The experimental IRSE data were analyzed assuming an isotropically-averaged effective electron mass parameter of $m^* = 0.28\,m_\mathrm{e}$ [135].[6] Thereupon, the free-charge-carrier concentration N and the optical mobility parameters μ_i^{opt} ($i = ||, \perp$) were obtained [43]. The results of the IRSE-analysis of two sets of Ga-doped ZnO thin films are summarized in Fig. 3.18.

For comparison, the results of electrical Hall-effect measurements performed on the same samples are also included in Fig. 3.18. Both sample sets reveal increasing free-charge-carrier concentration and free-charge-carrier mobility parameters with decreasing oxygen pressure and a maximum free-charge-carrier concentration of about $N \sim 4 \times 10^{19}\mathrm{cm}^{-3}$. N and $\mu_{||}$ obtained by IRSE and Hall-effect agree reasonably well. Note that the Hall-effect measures for *c*-plane orientation $\mu_\perp$ only. For (0001) ZnO thin films, IRSE analysis revealed an anisotropy of the mobility parameters, which was found to fulfill always the relation $\mu_{||}^{\mathrm{opt}} < \mu_{\perp}^{\mathrm{opt}}$.

Figure 3.19 depicts IRSE spectra of two magnetron-sputtered polycrystalline Al-doped ZnO thin films with high and extremely-high N values. Because of the large electron density of $N = 1 \times 10^{21}\mathrm{cm}^{-3}$, the strong plasmon contribution to the DF in the IR range completely screens the polar lattice mode excitation in this sample.

In highly-doped samples, or samples with codoping, it is often found that free charge carriers are not homogeneously distributed across the layer depth, but rather adopt a certain concentration profile. Figures 3.20a,b depict IRSE spectra of a Cu-doped ZnO thin film, together with two different best-model calculated data sets. In Fig. 3.20a, two layers were included into the model calculation, allowing for independent free-charge-carrier parameters within the two sublayers, whereas the phonon-mode parameters within the two layers share a common set. Figure 3.20b shows best-model calculations assuming

[6] It is implied that the inverse conduction band effective mass tensor does not depend on the wavevector $\boldsymbol{k}$, and that the inverse effective mass tensor renders the unit matrix times a $\boldsymbol{k}$-independent scalar parameter $(m^\star)^{-1}$.

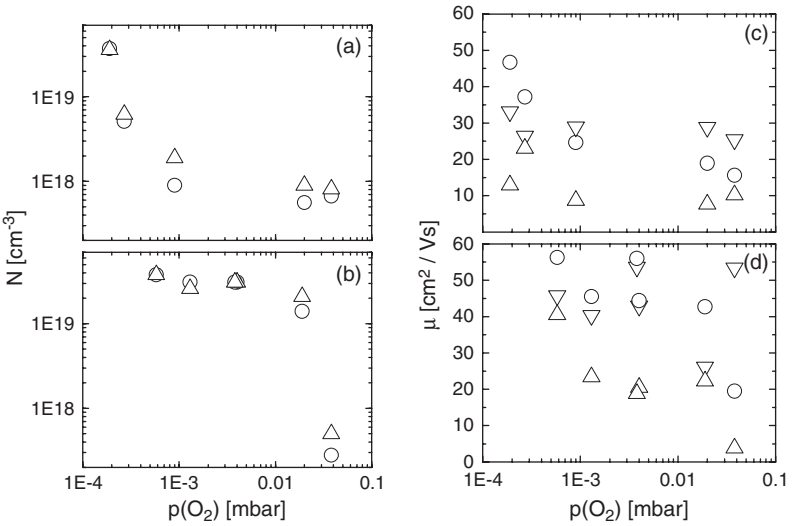

Fig. 3.18. Free-charge-carrier concentration (**a,b**) and mobility parameters (**c,d**) of Ga-doped ZnO thin films on sapphire vs. oxygen pressure during PLD-growth [43]. *Triangles* and *circles* correspond to the results determined by IRSE and Hall-effect measurements, respectively. Panels (**a,c**) and (**b,d**) contain the results of the films grown with 0.1 and 0.5 mass percent Ga_2O_3 powder within the PLD target, respectively. Up- and down-triangles in panels (**c**) and (**d**) represent the anisotropic optical mobility parameter $\mu_{||}^{\mathrm{opt}}$ and $\mu_{\perp}^{\mathrm{opt}}$, respectively

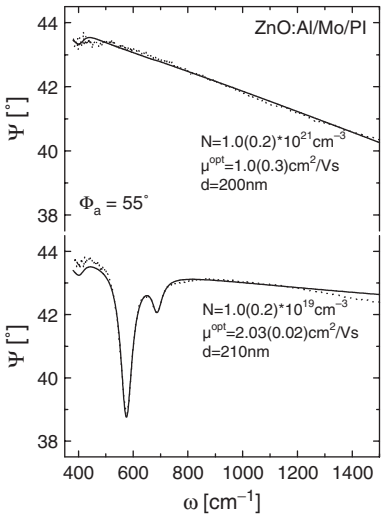

Fig. 3.19. Experimental (*dotted lines*) and best-model (*solid lines*) IRSE spectra of two polycrystalline Al-doped ZnO thin films grown by magnetron sputtering on metallized polyimide foil [43]. The best-model free-charge-carrier concentration, optical mobility, and thickness parameters are indicated

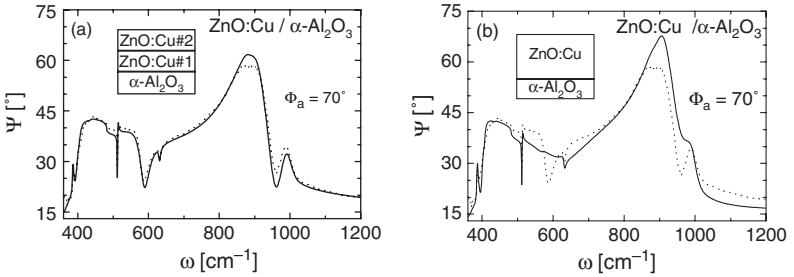

Fig. 3.20. Experimental (*dotted lines*) and best-model (*solid lines*) IRSE spectra of a PLD-grown Cu-doped ZnO thin film ($d \sim 1450\,\mathrm{nm}$) on sapphire [43]. Panel (**a**) contains the best-model calculation, which is obtained by dividing the ZnO layer into two sublayers with different free-charge-carrier parameters, as sketched in the inset. The best-model free-charge-carrier parameters in sublayer ♯1 ($d \sim 900\,\mathrm{nm}$) are $N = (8.15 \pm 0.01) \times 10^{18}\,\mathrm{cm}^{-3}$, $\mu_{\perp}^{\mathrm{opt}} = (32.5 \pm 0.3)\,\mathrm{cm}^2\,\mathrm{V}\,\mathrm{s}^{-1}$, and $\mu_{||}^{\mathrm{opt}} = (29.9 \pm 0.4)\,\mathrm{cm}^2\,\mathrm{V}^{-1}\,\mathrm{s}^{-1}$. The free-charge-carrier concentration in sublayer ♯2 ($d \sim 550\,\mathrm{nm}$) is below the IRSE detection limit of $N \sim 5 \times 10^{17}\,\mathrm{cm}^{-3}$. Panel (**b**) contains the best-model data, which are obtained by modeling the ZnO thin film as one homogeneous layer

a single layer for this sample. As can be seen, the best-model calculation improved considerably upon inclusion of a second layer, where it turns out that a large free-charge-carrier depleted zone (depletion layer) has formed near the top of the deposited thin film [43].

3.6 Below-Band-Gap Index of Refraction

3.6.1 ZnO

Figure 3.21a,c shows the index-of-refraction spectra $n_{||}$ and $n_{\perp}$ of ZnO below the fundamental band gap. The dispersion of the spectra can be described by the Cauchy formula [117]

$$n_i(x,\lambda) = \sum_{k=0}^{2} \left[A_i^{(k)} x^k + \frac{B_i^{(k)} x^k}{\lambda^2} + \frac{C_i^{(k)} x^k}{\lambda^4} \right], \tag{3.24}$$

where λ denotes the vacuum wavelength and i indicates the two polarization directions ($i = ||, \perp$). The parameter x describes the composition dependencies of the Cauchy parameters for $\mathrm{Mg}_x\mathrm{Zn}_{1-x}\mathrm{O}$ compounds (Sect. 3.6.2). The use of the Cauchy formulae requires a high-frequency (short-wavelength) limitation, which is approximated here by 90% of the respective fundamental band-to-band transition energy (band gap energy). The parameter A_i is equal to $\sqrt{\varepsilon_{\infty,i}}$, ignoring finite absorption due to defect- or impurity-related

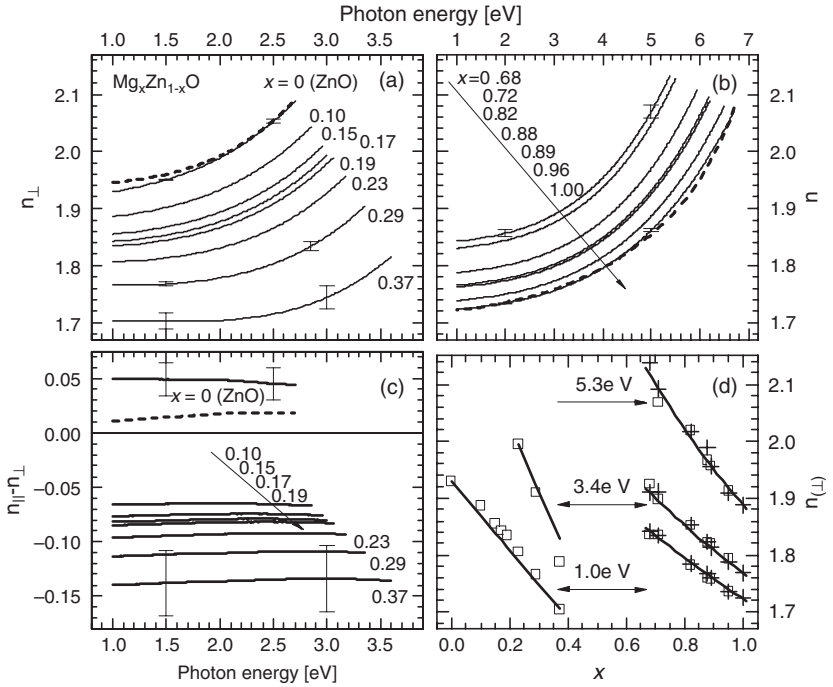

Fig. 3.21. Index-of-refraction spectra of PLD-grown ZnO and $Mg_xZn_{1-x}O$ thin films. (**a**) and (**b**): $n_\perp$ for wurtzite-structure and n for rocksalt-structure $Mg_xZn_{1-x}O$, respectively. (**c**) Birefringence $n_\parallel$–$n_\perp$ for wurtzite-structure $Mg_xZn_{1-x}O$. For some of the curves error bars are indicated. (**d**): $n_\perp$ ($x < 0.45$) and n ($x > 0.6$) for selected photon energies according to (3.24) and Tables 3.7 and 3.8 (*solid lines*), and experimental data points (*symbols*) from individual thin film samples. The *dashed lines* in panels (**a**) and (**c**) represent values from an *a*-plane ZnO single crystal bulk sample [121], and in panel (**b**) from an MgO single crystal bulk sample [136]. Reprinted with permission from [15, 16]

below-band-gap transitions. The Cauchy-parameters of ZnO are summarized in Table 3.7.

The birefringence, which is defined by $\Delta n = n_\parallel - n_\perp$, is positive with reported values ranging from $\Delta n = 0.001$ to $\Delta n = 0.05$ [15, 76, 95, 121, 124, 137]. Figure 3.22 plots the temperature derivative dn/dT for $n_\perp$ within the temperature range from $T = 40\,K$ to $T = 800\,K$ with an almost linear increase of $dn_\perp/dT$ with photon energy.

3.6.2 $Mg_xZn_{1-x}O$

Typical index-of-refraction spectra of $Mg_xZn_{1-x}O$ thin films with wurtzite and rocksalt structure are plotted in Figs. 3.21a–d. Data for $0 \le x \le 1$ originate from thin film measurements, those for $x = 0$ and $x = 1$ are

Table 3.7. Cauchy parameters (3.24) for wurtzite-structure ZnO and $Mg_xZn_{1-x}O$

			$A_i^{(0)}$	$A_i^{(1)}$	$B_i^{(0)}$ ($10^{-2}\,\mu m^2$)	$B_i^{(1)}$	$C_i^{(0)}$ ($10^{-3}\,\mu m^4$)	$C_i^{(1)}$
Mollwo (1954)	[137][a]	$n_\parallel$	2.001		−2.08		9.8	
		$n_\perp$	1.991		−2.52		10.5	
Bond (1965)	[124][a]	$n_\parallel$	1.925		3.05		1.61	
		$n_\perp$	1.911		2.91		1.74	
Hu (1997)	[138][b]	$n_\perp$	1.9281		−0.0011		5.97	
Yoshikawa (1997)	[76][a]	$n_\parallel$	1.962		−1.19		9.4	
		$n_\perp$	1.961		−2.10		11.5	
Jellison (1998)	[121][a]	$n_\parallel$	1.947		1.18		4.7	
		$n_\perp$	1.939		0.63		5.4	
Sun (1999)	[79][b]	n	1.909		1.51		4.7	
Teng (2000)	[95][c]	$n_\parallel$	1.915	−0.26	2.92	−2.9	1.7	−3.0
		$n_\perp$	1.899	−0.25	2.85	−3.2	1.6	−3.1
Schmidt (2003)	[15][b]	$n_\parallel$	1.966		1.81		3.6	
		$n_\perp$	1.916		1.76		3.9	
Schmidt (2003)	[15][d]	$n_\parallel$	1.844	−0.78	1.81	−4.5	3.6	−4.9
		$n_\perp$	1.916	−0.57	1.76	−4.5	3.9	−4.9

[a] ZnO single crystal bulk
[b] ZnO thin film
[c] $Mg_xZn_{1-x}O$ thin films with $0 \le x \le 0.36$
[d] $Mg_xZn_{1-x}O$ thin films with $0.1 \le x \le 0.37$

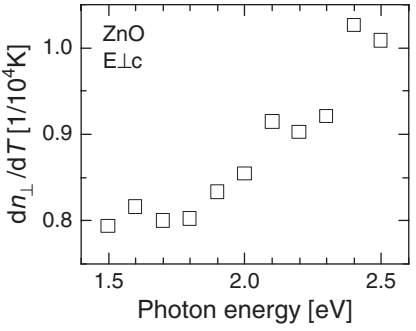

Fig. 3.22. Temperature dependence $dn_\perp/dT$ of the index of refraction of ZnO below the band gap for selected photon energies, as determined in the temperature range from $T = 60\,K$ to $T = 800\,K$. $dn_\perp/dT$ was found to be nearly constant in the studied temperature range

supplemented by data from single-crystal bulk samples. The corresponding Cauchy parameters are listed in Tables 3.7 and 3.8. In general, with increasing x, the indices of refraction decrease. Figure 3.21c shows the birefringence spectra. For $x \ge 0.1$, Δn is negative [15], in contrast to ZnO (Sect. 3.6.1), and increases with increasing Mg content x. Figure 3.21d shows the composition

Table 3.8. Same as Table 3.7 for rocksalt-structure $Mg_xZn_{1-x}O$

		$A_i^{(0)}$	$A_i^{(1)}$	$A_i^{(2)}$	$B_i^{(0)}$	$B_i^{(1)}$	$B_i^{(2)}$	$C_i^{(0)}$	$C_i^{(1)}$	$C_i^{(2)}$
					$(10^{-2}\,\mu m^2)$			$(10^{-3}\,\mu m^4)$		
Chen (2005)	[139][a]	2.016	−0.485	0.160	0.7	1.7	−1.8	1.9	−2.5	0.7
Schmidt-Grund (2006)	[16][b]	2.146	−0.508	0.083	1.6	−2.5	1.3	1.38	−1.48	0.36

[a] $Mg_xZn_{1-x}O$ thin films with $0.57 \leq x \leq 1$
[b] $Mg_xZn_{1-x}O$ thin films with $0.68 \leq x \leq 1$

dependence of the index of refraction, exemplarily, for three different photon energies [15, 16]. In analogy to the discontinuous composition dependence of the static and "high-frequency" dielectric constants (Sect. 3.3), the phonon-mode frequencies (3.4.3), and the fundamental band-to-band transition energies E_0^α (Sect. 3.7.2), the index of refraction reveals a strong discontinuity and increment upon phase transition. Note that second-order Cauchy coefficients are required to describe the composition dependence of the index of refraction for the rocksalt-structure compounds.

Sum rule considerations [140] imply that the discontinuity in the refractive index must be accompanied by a substantial increase of the oscillator strengths of higher energy transitions above the spectral range, from which data are available ($E < 10\,\text{eV}$). Otherwise the discontinuity of the lowest band-to-band transition energy (Sect. 3.7) would cause a decrease in the refractive index if the oscillator strengths within the rocksalt-structure part of the alloy would remain comparable to those within the wurtzite-structure part.

3.7 Band-to-Band Transitions and Excitonic Properties

3.7.1 ZnO

3.7.1.1 Band-to-Band Transitions

The DF spectra of wurtzite-structure ZnO within the VIS-to-VUV spectral region contain CP structures, which can be assigned to band-gap-related electronic band-to-band transitions E_0^α with $\alpha = A, B, C$ and to above-band-gap band-to-band transitions E^β with $\beta = 1, \ldots, 7$. The E_0^α-related structures can be described by lineshape functions of the 3DM_0-type (3.9 and 3.10), the CP structures with $\beta = 3, 4$ by lineshape functions of the 2DM_0-type (3.11), and the CP structures with $\beta = 1, 2, 5, 6, 7$ can be described by Lorentzian-damped harmonic oscillator functions (3.13). The CP structures E_0^α are supplemented by discrete (3.14) and continuum (3.16) excitonic contributions. Tables 3.9 and 3.10 summarize typical parameters of the CPs E_0^α and E^β, respectively, of ZnO [15].

Table 3.9. Typical energy, amplitude, and broadening parameters of near-band-gap CP structures E_0^α ($\alpha = A$, B, and C) and their exciton polarizabilities of ZnO obtained from SE analysis of multiple sample sets at RT

		$\varepsilon_\perp$	$\varepsilon_\parallel$
E_0^A	(eV)	3.366 ± 0.004	
A_0^A	($eV^{3/2}$)	6.5 ± 1.1	1.5 ± 1.3
A_{xc}^A	(eV^2)	0.33 ± 0.02	0.03 ± 0.03
$A_{xb}^{1,A}$	(eV)	0.023 ± 0.003	0.015 ± 0.010
E_0^B	(eV)	3.380 ± 0.004	
A_0^B	($eV^{3/2}$)	1.5 ± 1.1	0.0 ± 1.0
A_{xc}^B	(eV^2)	0.097 ± 0.016	0.00 ± 0.10
$A_{xb}^{1,B}$	(eV)	0.044 ± 0.009	0.000 ± 0.010
E_0^C	(eV)	3.434 ± 0.018	
A_0^C	($eV^{3/2}$)	0.21 ± 0.4	1.6 ± 0.8
A_{xc}^C	(eV^2)	0.017 ± 0.015	0.57 ± 0.07
$A_{xb}^{1,C}$	(eV)	0.026 ± 0.008	0.078 ± 0.009
E_{xb}^1	(eV)	0.060 ± 0.002	
$\Gamma_0 \sim \Gamma_{xc} \sim \Gamma_{xb}$	(eV)	0.020 ± 0.009	

Table 3.10. Same as Table 3.9 for CP structures E^β ($\beta = 1 \ldots 7$)

	$\varepsilon_\perp$	$\varepsilon_\parallel$
E^1 (eV)	5.494 ± 0.063	5.268 ± 0.09
A^1	0.50 ± 0.08	0.22 ± 0.13
Γ^1 (eV)	3.6 ± 0.6	3.0 ± 0.8
E^2 (eV)	6.494 ± 0.02	6.419 ± 0.17
A^2	0.16 ± 0.03	0.06 ± 0.01
Γ^2 (eV)	1.0 ± 0.1	0.53 ± 0.09
E^3 (eV)	7.135 ± 0.021	7.086 ± 0.013
A^3	0.34 ± 0.04	0.09 ± 0.02
Γ^3 (eV)	0.29 ± 0.02	0.11 ± 0.02
E^4 (eV)	7.537 ± 0.040	7.341 ± 0.015
A^4	0.18 ± 0.06	0.07 ± 0.01
Γ^4 (eV)	0.32 ± 0.03	0.10 ± 0.03
E^5 (eV)	–	8.167 ± 0.044
A^5	–	0.55 ± 0.04
Γ^5 (eV)	–	1.95 ± 0.15
E^6 (eV)	8.707 ± 0.005	8.881 ± 0.005
A^6	0.48 ± 0.05	0.85 ± 0.04
Γ^6 (eV)	1.03 ± 0.08	1.05 ± 0.03
E^7 (eV)	9.044 ± 0.008	–
A^7	0.13 ± 0.04	–
Γ^7 (eV)	0.49 ± 0.08	–

3.7.1.2 Γ-Point Fundamental Band-to-Band Transition

The fundamental absorption edge in ZnO corresponds to the direct transition from the highest valence band to the lowest conduction band at the Γ-point of the Brillouin zone [141]. RT-data for the energy of the lowest Γ-point band-to-band transition are summarized in Table 3.11.

3.7.1.3 Γ-Point Valence-Band Ordering

The lowest conduction band of ZnO exhibits Γ_7-symmetry. The highest valence band of ZnO is split into two bands with Γ_7- and one band with Γ_9-symmetry due to the spin-orbit and crystal-field interactions [76,154–158]. The corresponding three lowest Γ-point band-to-band transition energies are denoted here by E_0^α. So far, the order of the highest valence bands of unstrained ZnO, Γ_7-Γ_9-Γ_7 (Γ_{797}) or Γ_9-Γ_7-Γ_7 (Γ_{977}), is still a subject of debate [157, 158]. The RT properties of the E_0^α-band-to-band transitions of ZnO thin films deposited on sapphire substrate were reported as follows: Although for $\varepsilon_\perp$ all amplitude parameters A_0^A, A_0^B, and A_0^C are finite, for $\varepsilon_\parallel$ the E_0^B transition is suppressed ($A_0^B = 0$) in agreement with theoretical predictions for the case of the valence-band order Γ_{797}, where transitions between the conduction band and the valence band with Γ_9-symmetry are forbidden to couple to photons polarized perpendicular to the optical c-axis [76].

3.7.1.4 Crystal-Field Splitting and Spin–Orbit Coupling Parameters

The quasi-cubic model approximation can be invoked to calculate the crystal-field splitting (Δ_{cf}) and spin-orbit coupling (Δ_{so}) parameters from E_0^α [76, 159, 160]

$$\Delta_{\mathrm{cf}} = -\frac{1}{2}\left(\Delta_{12} - \Delta_{13} + \sqrt{(\Delta_{12}+\Delta_{13})^2 - 6\Delta_{12}\Delta_{13}}\right), \tag{3.25}$$

$$\Delta_{\mathrm{so}} = -\frac{1}{2}\left(\Delta_{12} - \Delta_{13} - \sqrt{(\Delta_{12}+\Delta_{13})^2 - 6\Delta_{12}\Delta_{13}}\right), \tag{3.26}$$

where $\Delta_{ij} = E_0^{\alpha_i} - E_0^{\alpha_j}$ are the valence-band splitting energies. Reported Δ_{cf}- and Δ_{so}-values for ZnO are summarized in Table 3.12.

3.7.1.5 Excitonic Properties

Discrete and continuum free exciton contributions can be identified for each of the band-to-band transitions E_0^α. Sharp resonance features are superimposed to each of the E_0^α CP structures because of discrete exciton lines, where the ground and first excited state ($n = 1, 2$) can be seen at RT, and the second

Table 3.11. RT-data for E_0^α (lowest Γ-point band-to-band transitions) and E_g (fundamental absorption edge determined from transmission measurements), and E_{xb}^1 of ZnO single crystal bulk samples (b) and ZnO thin films (f)

Ref.	Sample	E_g (eV)	E_0^A ($\varepsilon_\perp$) (eV)	E_0^A ($\varepsilon_\parallel$) (eV)	E_0^B (eV)	E_0^C (eV)	E_{xb}^1 ($\varepsilon_\perp$) (meV)	E_{xb}^1 ($\varepsilon_\parallel$) (meV)
Yoshikawa (1997)	[76] (b)		3.450	3.450	[a]	[b]	59	59
Jellison (1998)	[121] (b)		3.372	3.405			56	50
Washington (1998)	[78] (f)		3.372			60		
Muth (1999)	[142] (f)		3.40		3.45	3.55	[c]	
Kang (2000)	[90] (f)		3.34				60	
Rebien (2002)	[122] (f)		3.37					
Zhao (2002)	[96] (f)		3.4				60	
Djurisic (2003)	[143] (b)		3.406	3.445			72	73
Djurisic (2003)	[143] (b)		3.407	3.4889	[d]	[e]	90	78
Ozaki (2003)	[144] (b)		3.380		3.394	3.438	[f]	
Schmidt (2003)	[15] (f)		3.366		3.380	3.434	60	
Kang (2004)	[82] (b)		3.373	3.407			55.3	51.3
Kang (2004)	[82] (f)		3.378	3.413			61.1	72.8
Srikant (1997)	[145] (f)	3.24 ... 3.32						
Ohtomo (1998)	[11] (f)	3.29						
Studenikin (1998)	[146] (f)	3.195 ... 3.370						
Paraguay (1999)	[147] (f)	3.28						
Meng (2000)	[148] (f)	3.21						
Minemoto (2000)	[99] (f)	3.24						
Postava (2000)	[80] (f)	3.35 ... 3.44					45... 71	
Santana (2000)	[149] (f)	3.28						
Park (2002)	[87] (f)	3.25						
Tokumoto (2002)	[150] (f)	3.28						
Takeuchi (2003)	[98] (f)	3.28						
Chen (2003)	[100] (f)	3.273						
Shan (2003)	[151] (f)	3.25 ... 3.28						
Misra (2004)	[152] (f)	3.28						
Shan (2004)	[97] (f)	3.274						
Zhao (2005)	[153] (f)	3.25 ... 3.27						

[a] $E_{xb}^{1,\alpha}$ with $\alpha = A$, B, and C is 68, 65, and 63 meV, respectively
[b] $\varepsilon_\perp$: 3.471 eV, $\varepsilon_\parallel$: 3.432 eV
[c] $\varepsilon_\perp$: 3.548 eV
[d] $\varepsilon_\perp$: 3.453 eV
[e] $\varepsilon_\perp$: 3.484 eV, $\varepsilon_\parallel$: 3.484 eV
[f] $E_{xb}^{1,\alpha}$ with $\alpha = A$, B, and C is 63.1, 50.4, and 48.9 meV, respectively

exited state ($n = 3$) evolves at low temperatures (3.15, Figs. 3.5, 3.23 [15]). It is often assumed that $E_{xb}^n := E_{xb}^{n,A} = E_{xb}^{n,B} = E_{xb}^{n,C}$ for transitions E_0^α. Table 3.11 summarizes data reported for E_{xb}^1 by various authors. An MDF parameter set for the exciton contributions to the DF is listed in Table 3.9.

Table 3.12. Crystal-field splitting (Δ_{cf}) and spin-orbit coupling (Δ_{so}) energies for ZnO single crystal bulk samples (b) and ZnO thin films (f) depending on the assumed valence-band ordering[a]

Ref.		Sample	Temp.	Valence-band ordering	Δ_{cf} (meV)	Δ_{so} (meV)
Liang (1968)	[161]	(b)	RT	Γ_{797}	40.8	−4.7
Langer (1970)	[162]	(b)	RT	Γ_{977}	43	19
Reynolds (1999)	[163]	(b)	RT	Γ_{977}	43	16
Mang (1995)	[164]	(b)	RT	Γ_{797}	39.4	−3.5
Srikant (1997)	[145]	(f)	RT	Γ_{797}	42	−5
Ozaki (2003)	[144]	(b)	RT	Γ_{977}	45	27
Ozaki (2003)	[144]	(b)	RT	Γ_{797}	49	−19
Schmidt-Grund	(unpubl.)	(f)	RT → 5K	$\Gamma_{977} \rightarrow \Gamma_{797}{}^{\dagger}$	50 → −82	19 → 16
Schmidt-Grund	(unpubl.)	(f)	RT → 5K	$\Gamma_{797} \rightarrow \Gamma_{977}{}^{\dagger}$	51 → −82	−15 → −18

[a] Regardless of the assumed valence-band ordering, Δ_{cf} is positive at RT and negative at $T = 5\,\mathrm{K}$. This implies that the valence-band ordering must change (†) due to temperature-induced biaxial-strain variation

The amplitude parameter selection rules for the discrete and continuum exciton contributions were found concordant with those of the E_0^{α} transitions.

3.7.1.6 Temperature Influence on the Γ-Point Transitions

The Γ-point transition energies shift to lower energies with increasing temperature. The energy shift is accompanied by a continuous lineshape broadening, and is caused mainly by the increase in electron–phonon interaction.

The influence of the electron–phonon interaction on the band-to-band transition energies E_0^{α} at low temperatures is often addressed by the Varshni equation [165]

$$E_0^{\alpha}(T) = E_0^{\alpha}(0) - \frac{\alpha_V T^2}{T + \theta_D}\,. \tag{3.27}$$

$E_0^{\alpha}(0)$ is the transition energy at $T = 0\,\mathrm{K}$, α_V is a model parameter, and θ_D is the Debye temperature.

At higher temperatures the semiempirical Bose–Einstein model function can be applied [129, 166]

$$E_0^{\alpha}(T) = E_0^{\alpha}(0) - \frac{\alpha_{BE}\theta_{BE}}{\exp(\theta_{BE}/T) - 1}, \tag{3.28}$$

which assumes an effective phonon-mode temperature θ_{BE}. $E_0^{\alpha}(0)$ is again the transition energy at $T = 0\,\mathrm{K}$, α_{BE} is a model parameter. Reported parameters for the Varshni and the Bose–Einstein model for ZnO bulk samples are given in Table 3.13.

It was pointed out that contributions due to acoustical and optical phonons must be considered for ZnO [169–172]. This is done by the two-oscillator model [169, 173]

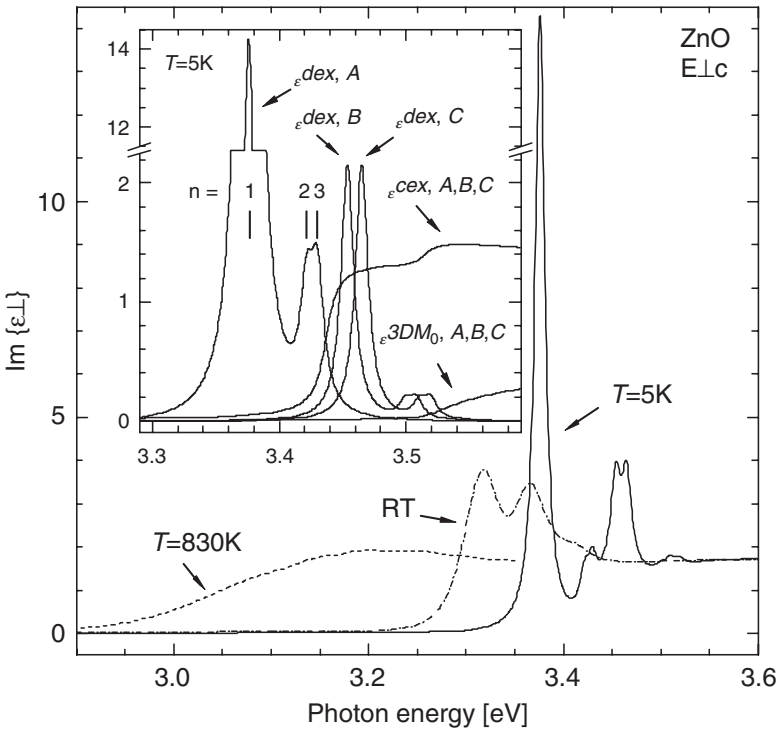

Fig. 3.23. $\mathrm{Im}\{\varepsilon_\perp\}$ of a PLD-grown ZnO thin film at $T = 5\,\mathrm{K}$, RT, and $T = 830\,\mathrm{K}$ in the photon energy range of the lowest Γ-point band-to-band transitions determined by SE. The inset depicts the contributions of the discrete ($\varepsilon^{\mathrm{dex},A,B,C}$) and the continuum ($\varepsilon^{\mathrm{cex},A,B,C}$) exciton polarizabilities and the lowest Γ-point band-to-band transitions ($\varepsilon^{3\mathrm{D}M_0,A,B,C}$) at $T = 5\,\mathrm{K}$. The ground, first, and second excited exciton states ($n = 1, 2, 3$) are labeled (3.15). Note the axis brake in the inset. Reprinted with permission from [85]

Table 3.13. Parameters of the temperature dependence of E_0^A according to the Varshni and Bose–Einstein model for ZnO single crystal bulk samples

		Varshni-model			Bose–Einstein-model		
Ref.		$E_0^A(0\,\mathrm{K})$ (eV)	α_V ($10^{-4}\mathrm{eV\,K^{-1}}$)	θ_D (K)	$E_0^A(0\mathrm{K})$ (eV)	α_BE ($10^{-4}\mathrm{eV\,K^{-1}}$)	θ_BE (K)
Boemare (2001)	[167]	3.4407	6.7	672	3.436	2.5	203
Ozaki (2003)	[144]	3.441	6.5	660			
Wang (2003)	[168]	3.440	8.2	700	3.440	3.75	240

$$E_0^\alpha(T) = E_0^\alpha(0) - \alpha_{2\mathrm{O}} \sum_{i=1}^{2} \frac{W_i \theta_i}{\exp(\theta_i/T) - 1}\,, \tag{3.29}$$

which describes the electron–phonon coupling in ZnO for both low and high temperatures. θ_i are the associated phonon temperatures, and W_i represent

Table 3.14. Parameters of the temperature dependence of the transition energy E_0^A and the discrete free exciton FWHM W_{2O} according to the 2-oscillator model for a ZnO thin film[a]

E_0^A/W_{2O}	$E_0^A(0)/W_{2O}(0)$ (eV)	α_{2O} (10^{-4}eV K^{-1})	W_1	θ_1 (K)	θ_2 (K)	θ_{2O} (K)	δ	θ_D (K)
E_0^A	3.4365	4.1	0.30	145	529	414	0.42	621
	(0.0004)	(0.1)	(0.05)	(25)	(30)	(28)	(0.10)	(42)
W_{2O}	0.0124	2.8	0.27	129	680	531	0.46	797
	(0.0010)	(0.5)	(0.18)	(50)	(50)	(50)	(0.12)	(75)

[a] Note that $W_2 = 1 - W_1$; Numbers in parenthesis are error bars

their relative weight. $E_0^\alpha(0)$ is the transition energy at $T = 0\,\mathrm{K}$. α_{2O} is the slope of the energy shift at temperatures far above the highest phonon temperature.[7] Figure 3.25b depicts $E_0^A(T)$-data obtained from a (0001) ZnO thin film on (0001) sapphire together with the best-model calculation according to (3.29) with k=2. The best-model parameters are given in Table 3.14. Here, the $E_0^A(0)$-data are not corrected for an energy shift, which originates in the thermal-expansion-mismatch induced biaxial strain[8] between the ZnO thin film and the substrate. The phonon energy of the first branch $k_B\theta_1 \sim 13\,\mathrm{meV}$ ($\omega \sim 101\,\mathrm{cm}^{-1}$) falls into the range of the acoustical phonon branch of ZnO [106, 174, 175]. The energy of the second phonon branch $k_B\theta_2 \sim 46\,\mathrm{meV}$ ($\omega \sim 368\,\mathrm{cm}^{-1}$) is in good agreement with the phonon-band-edge, i.e., close to the energy of the lowest occupied states of the high-energy ZnO optical phonon branch. The latter extends from about 47 meV ($\omega[A_1(\mathrm{TO})] = 380\,\mathrm{cm}^{-1}$) to about 73 meV ($\omega[E_1(\mathrm{LO})] = 588\,\mathrm{cm}^{-1}$) [38]. Calculations of the phonon density of states showed a strong maximum at the lower part of the upper phonon branch [174]. According to $W_1 = 0.30$ and $W_2 = 0.70$ optical phonons contribute much stronger to the temperature dependence of E_0^A than acoustical phonons. The Debye-temperature can be estimated by $\theta_D \sim (3/2)\theta_{2O}$ [176]. Tables 3.14 summarizes the parameters for the temperature dependence of E_0^A for a ZnO thin film.

The electron–phonon interactions also influence the linewidth of the interband and exciton transitions. This temperature-dependent homogeneous

[7] An effective phonon temperature can be defined, e.g., for k=2, by the weighted mean-value of the discrete phonon temperatures, $\theta_{2O} \equiv W_1\theta_1 + W_2\theta_2$. The material-related parameter $\delta = \sqrt{(\theta_2 - \theta_{2O})(\theta_{2O} - \theta_1)}/\theta_{2O}$ can be used to distinguish between weak ($\delta < 0.33$), intermediate ($0.33 \leq \delta \leq 0.577$), and strong coupling regimes ($\delta > 0.57$) [173]. For ZnO the coupling regime is intermediate (Table 3.14).

[8] Of more subtle influence is the biaxial strain in thin film samples, which is introduced upon different thermal expansion coefficients for the film and the substrate material. Furthermore, the biaxial strain can depend on the growth history. On this matter the amount of available information is not exhaustive.

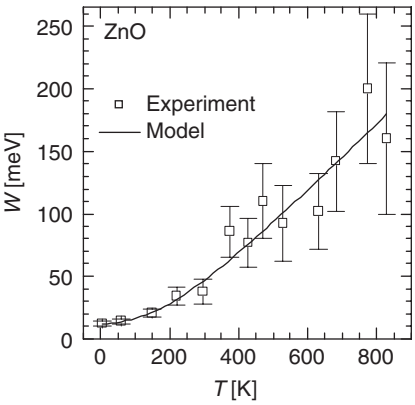

Fig. 3.24. Experimental data (*symbols*) of the FWHM W of the discrete free exciton together with model calculations (*solid line*) according to the two-oscillator model ($W_{2O}(T)$, 3.30) vs. temperature of a ZnO thin film

broadening is superimposed by the (often assumed) temperature-independent lifetime and inhomogeneous broadening due to exciton-, disorder-, and defect-induced exciton scattering. Within the 2-oscillator model, the temperature dependence of the full width at half maximum value (FWHM) W can be described, similarly to the temperature dependence of the fundamental band-to-band transition energy [177], by

$$W_{2O}(T) = W_{2O}(0) - \alpha_{2O} \sum_{i=1}^{2} \frac{W_i \theta_i}{\exp(\theta_i/T) - 1} \tag{3.30}$$

with $W_{2O}(T = 0\text{K}) = W_{2O}(0)$ and all other parameters as defined in (3.29). Figure 3.24a depicts the temperature dependence of W for the E_0^A exciton line and the best-model calculation according to (3.30). The experimental data were obtained from MDF analysis of temperature-dependent SE spectra taken from a (0001) ZnO thin film on (0001) sapphire. The corresponding parameters α_{2O}, W_i, and θ_i are summarized in Table 3.14. The best-model free-exciton FWHM at $T = 0\,\text{K}$ is $W_{2O}(0) = 12.4 \pm 1\,\text{meV}$. This value is larger than the FWHM value of $\sim 2 \ldots 5\,\text{meV}$ for the donor bound exciton measured by low-temperature cathodoluminescence and photoluminescence excitation spectroscopy [15, 19]. Figure 3.25a shows the temperature dependence of the E_0^α transition energy parameters. At high temperatures the slope is linear. Table 3.15 summarizes $(\partial E_0^\alpha/\partial T)|_{T\to\infty}$ and $(\partial E_g/\partial T)|_{T\to\infty}$ data for ZnO. Superimposed on the electron–phonon coupling-induced band shift are again effects due to thermal-induced biaxial strain, which effects the crystal-field splitting parameter. The spin-orbit coupling parameter should depend only slightly on temperature.

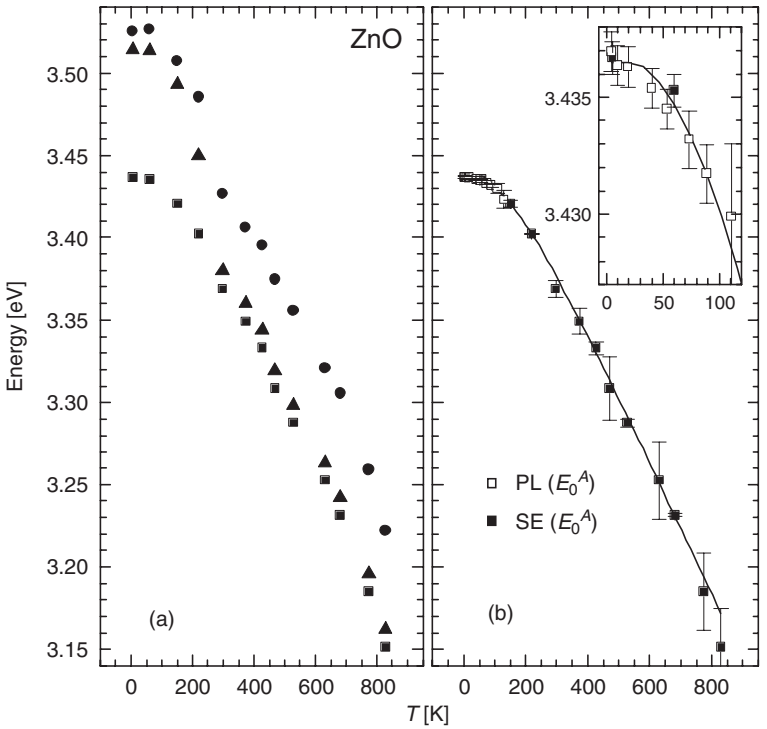

Fig. 3.25. (a): Γ-point band-to-band transition energies E_0^{A} (squares), E_0^{B} (triangles), and E_0^{C} (circles) of a PLD-grown ZnO thin film as a function of temperature obtained by SE. (b) Data for E_0^{A} from SE (solid symbols) and low-temperature PL (open symbols), and model calculations according to (3.29) (solid line). The inset enlarges the temperature range $T \leq 120\,\mathrm{K}$.

Table 3.15. High-temperature slope $(\partial E_0^{\alpha}/\partial T)|_{T\to\infty}$ in units of $10^{-4}\,\mathrm{eV\,K^{-1}}$ of ZnO single crystal bulk samples (b) and ZnO thin films (f)

Ref.		Sample	E_0^{A}	E_0^{B}	E_0^{C}	E_{g}
Watanabe (1964)	[178]	(b)				−8
Ozaki (2003)	[144]	(b)	−3.4	−3.4	−3.4	
Ozaki (2003)	[144]	(b)	−2.9	−2.9	−2.9	
Schmidt-Grund (unpubl.)		(f)	−4.3	−4.3	4.1	

3.7.2 $\mathbf{Mg_xZn_{1-x}O}$

3.7.2.1 Γ-Point Band-to-Band Transitions

$Mg_xZn_{1-x}O$ crystallizes in the wurtzite or in the rocksalt structure, depending on the Mg mole fraction x. The alloys remain direct-gap materials over the whole composition range. The wurtzite-structure part reflects a valence-band structure, which is similar to ZnO. For the rocksalt-structure part the

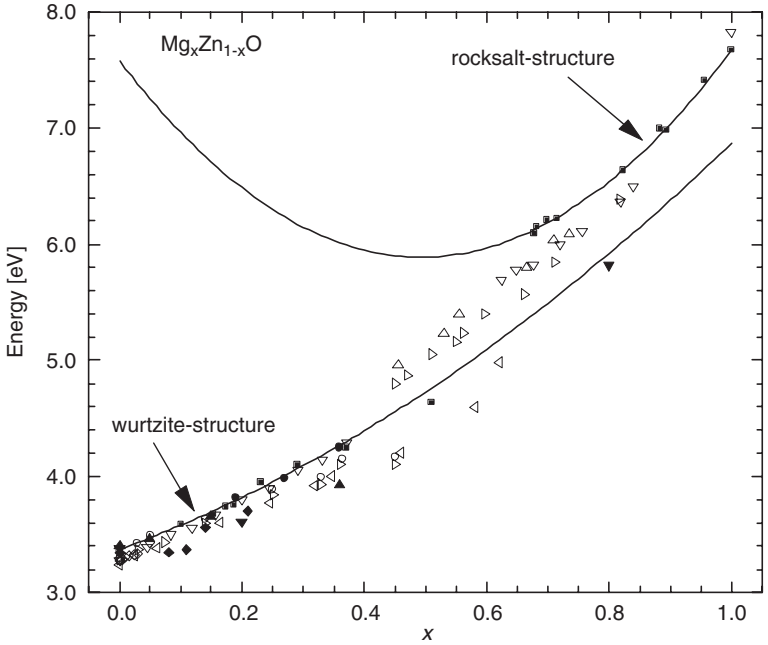

Fig. 3.26. Energies of the fundamental absorption edge E_g (*open symbols*) and the lowest Γ-point band-to-band transition E_0^A or E_0^D (*filled symbols*) of $Mg_xZn_{1-x}O$, as determined by transmission measurements (T) and SE, respectively. *Filled squares*: Refs. [15, 16] (SE), *filled circles*: [95] (T), *filled diamonds*: [90] (SE), *filled up-triangles*: [96] (T), *filled down-triangles*: [82] (SE), *open circles*: [11] (T), *open diamonds*: [97] (T), *open up-triangles*: [14] (T), *open down-triangles*: [98] (T), *open left-triangles*: [99] (T), *open right-triangles*: [100] (T). The lines depict numerical approximations according to (3.31) with the parameters in Table 3.16 for E_0^A (wurtzite-structure $Mg_xZn_{1-x}O$) and E_0^D (rocksalt-structure $Mg_xZn_{1-x}O$)

crystal-field splitting parameter vanishes, and the valence band is split into two bands only, with $E_0^D = E_0$ and $E^E = E_0 + \Delta_{so}$, and their CP structures can be well adopted by those of the 3DM_0-type (3.9). Figure 3.26 summarizes data of the band gap energies of $Mg_xZn_{1-x}O$ vs. x.

With increasing Mg-content the Γ-point band-to-band transitions shift to higher photon energies with a small bowing, which can be described by

$$E_0^\alpha(x) = E_0^\alpha(x=0) + p^\alpha x + q^\alpha x^2 \,. \tag{3.31}$$

The best-model parameters p^α and q^α from [15, 16] are given in Table 3.16.

The data in Table 3.16 may be used to estimate the band gap energy for unstrained wurtzite-structure MgO of $E_0^A = 6.9\,\text{eV}$ and for rocksalt-structure ZnO of $E_0^D = 7.6\,\text{eV}$, with stronger bowing for the rocksalt-structure than for the wurtzite-structure occurrence of the alloys. Theoretical band-structure calculations for ZnO revealed the high-pressure rocksalt-structure phase as

Table 3.16. Best-model parameters for the Mg-content dependence of the Γ-point band-to-band transition energies E_0^α (3.31) at RT [15, 16]

α	x	$E_0^\alpha(x=0)$ (eV)	p^α (eV)	q^α (eV)
A	$0 \ldots 0.51$	3.369 ± 0.002	1.93 ± 0.06	1.57 ± 0.25
B	$0 \ldots 0.51$	3.379 ± 0.003	2.0 ± 0.1	1.9 ± 0.4
C	$0 \ldots 0.23$	3.427 ± 0.007	2.2 ± 0.3	1.4 ± 0.9
D	$0.68 \ldots 1$	7.6 ± 0.5	-7 ± 1	7.0 ± 1
E	$0.68 \ldots 1$	8.0 ± 0.8	-7.5 ± 2	7.2 ± 1.5

an indirect gap material ($E_{\mathrm{ind}} \sim 5.4\,\mathrm{eV}$), for which the Γ-point band gap energy $E_0^D = 6.54\,\mathrm{eV}$ is predicted to be much larger than $E_0^A = 3.34\,\mathrm{eV}$ of the wurtzite-structure ZnO [121, 179, 180], which is in qualitative agreement with the extrapolation in Fig. 3.26.

Acknowledgement. The authors thank Prof. M. Grundmann, Prof. W. Grill, and Prof. B. Rheinländer (all Universität Leipzig) for continuing support and enlightening discussions. We acknowledge technical support by A. Rahm (XRD), D. Speman (RBS), U. Teschner (Raman), and H. v. Wenckstern (Hall, all Universität Leipzig), D. Faltermeier, Dr. B. Gompf, and Prof. M. Dressel (low temperature ellipsometry, all Universität Stuttgart), and Dr. C. M. Herzinger (VUV-ellipsometry, J. A. Woollam Co., Inc., Lincoln, Nebraska, USA). We thank H. Hochmuth, Dr. E. M. Kaidashev, G. Ramm, and Dr. M. Lorenz for the PLD-preparation (see Chap. 7) of most of the thin film samples studied in this chapter, and the Solarion GmbH Leipzig for providing magnetron sputtered thin film samples. Finally, we thank all current and former members of the Workgroup Ellipsometry at the Universität Leipzig for diverse support: N. Ashkenov, A. Carstens, T. Chavdarov, Dr. T. Hofmann, Dr. A. Kasic, Dr. G. Leibiger, B. N. Mbenkum, M. Saenger, and C. Sturm.

Financial support was provided by the German Federal Ministry of Education and Research BMBF (FK 03WKI09) and the German Research Foundation DFG (Grant No. SCHUH 1338/3-1, SCHUH 1338/4-1, SCHUH 1338/4-2, Gr 1011/10-1, and Gr 1011/14-1).

References

1. D.M. Bagnall, Y.F. Chen, Z. Zhu, T. Yao, S. Koyama, M.Y. Shen, T. Goto, Appl. Phys. Lett. **70**, 2230 (1997)
2. D.C. Reynolds, D.C. Look, B. Jogai, Solid State Commun. **99**, 873 (1996)
3. Y. Segawa, A. Ohtomo, M. Kawasaki, H. Koinuma, Z. Tang, P. Yu, G. Wong, Phys. Status Solidi B **202**, 669 (1997)
4. P. Zu, Z.K. Tang, G.K.L. Wong, M. Kawasaki, A. Ohtomo, H. Koinuma, Y. Segawa, Solid State Commun. **103**, 459 (1997)
5. Z.K. Tang, G.K.L. Wong, P. Yu, M. Kawasaki, A. Ohtomo, H. Koinuma, Y. Segawa, Appl. Phys. Lett. **72**, 3270 (1998)

6. W. Hirschwald, P. Bonasewicz, L. Ernst, M. Grade, D. Hofmann, S. Krebs, R. Littbarski, G. Neumann, M. Grunze, D. Kolb, H.J. Schulz, *Current Topics in Materials Science*, vol. 7 (North-Holland, Amsterdam, 1981)
7. I. Vurgaftman, J.R. Meyer, J. Appl. Phys. **94**, 3675 (2003)
8. D.M. Roessler, W.C. Walker, Phys. Rev. **159**, 733 (1967)
9. F. Koffyberg, Phys. Rev. B **13**, 4470 (1976)
10. D. Look, D. Reynolds, J. Sizelove, R. Jones, C. Litton, G. Cantwe, W. Harsch, Solid State Commun. **105**, 399 (1998)
11. A. Ohtomo, M. Kawasaki, T. Koida, K. Masubuchi, H. Koinuma, Y. Sakurai, Y. Yoshida, T. Yasuda, Y. Segawa, Appl. Phys. Lett. **72**, 2466 (1998)
12. A.K. Sharma, J. Narayan, J.F. Muth, C.W. Teng, C. Jin, A. Kvit, R.M. Kolbas, O.W. Holland, Appl. Phys. Lett. **75**, 3327 (1999)
13. T. Makino, Y. Segawa, M. Kawasaki, A. Ohtomo, R. Siroki, K. Tamura, T. Yasuda, H. Koinuma, Appl. Phys. Lett. **78**, 1237 (2001)
14. S. Choopun, R.D. Vispute, W. Yang, R.P. Sharma, T. Venkatesan, H. Shen, Appl. Phys. Lett. **80**, 1529 (2002)
15. R. Schmidt, B. Rheinländer, M. Schubert, D. Spemann, T. Butz, J. Lenzner, E.M. Kaidashev, M. Lorenz, A. Rahm, H.C. Semmelhack, M. Grundmann, Appl. Phys. Lett. **82**, 2260 (2003)
16. R. Schmidt-Grund, A. Carstens, B. Rheinländer, D. Spemann, H. Hochmut, M. Lorenz, M. Grundmann, C.M. Herzinger, M. Schubert, J. Appl. Phys. **99**, 123701 (2006)
17. T. Minami, MRS Bull. **25**(Aug), 38 (2000)
18. S.J. Pearton, D.P. Norton, K. Ip, Y.W. Heo, T. Steiner, Superlattice Microst. **34**, 3 (2003)
19. E.M. Kaidashev, M. Lorenz, H. von Wenckstern, G. Benndorf, A. Rahm, H.C. Semmelhack, K.H. Han, H. Hochmuth, C. Bundesmann, V. Riede, M. Grundmann, Appl. Phys. Lett. **82**, 3901 (2003)
20. M. Lorenz, E.M. Kaidashev, H.v. Wenckstern, V. Riede, C. Bundesmann, D. Spemann, G. Benndorf, H. Hochmuth, A. Rahm, H.C. Semmelhack, M. Grundmann, Solid State Electron. **43**, 2205 (2003)
21. E.C. Lee, K.J. Chang, Phys. Rev. B **70**, 115210 (2004)
22. D.C. Look, B. Claflin, Y.I. Alivov, S.J. Park, Phys. Status Solidi A **201**, 2203 (2004)
23. T. Dietl, H. Ohno, F. Matsukura, J. Cibert, D. Ferrand, Science **287**, 1019 (2000)
24. K. Ueda, H. Tabata, T. Kawai, Appl. Phys. Lett. **79**, 988 (2001)
25. K. Sato, H. Katayama-Yoshida, Jpn. J. Appl. Phys. **39**, L555 (2000)
26. Z. Jin, M. Murakami, T. Fukumura, Y. Matsumoto, A. Ohtomo, M. Kawasaki, H. Koinuma, J. Cryst. Growth **214–215**, 55 (2000)
27. H. Katayama-Yoshida, K. Sato, T. Yamamoto, Jpn. Soc. Appl. Phys. **6**, 20 (2002)
28. M. Diaconu, H. Schmidt, H. Hochmuth, M. Lorenz, G. Benndorf, J. Lenzner, D. Spemann, A. Setzer, K.W. Nielsen, P. Esquinazi, M. Grundmann, Thin Solid Films **486**, 117 (2004)
29. T. Gruber, G.M. Prinz, C. Kirchner, R. Kling, F. Reuss, W. Limmer, A. Waag, J. Appl. Phys. **96**, 289 (2004)
30. S. Heitsch, C. Bundesmann, G. Wagner, G. Zimmermann, A. Rahm, H. Hochmuth, G. Benndorf, H. Schmidt, M. Schubert, M. Lorenz, M. Grundmann, Thin Solid Films **496**, 234 (2006)

31. R. Callender, S. Sussman, M. Selders, R. Chang, Phys. Rev. B **7**, 3788 (1973)
32. T.C. Damen, S.P.S. Porto, B. Tell, Phys. Rev. **142**, 570 (1966)
33. C.A. Arguello, D.L. Rousseau, S.P.S. Porto, Phys. Rev. **181**, 1351 (1969)
34. J.F. Scott, Phys. Rev. B **2**, 1209 (1970)
35. J.M. Calleja, M. Cardona, Phys. Rev. B **16**, 3753 (1977)
36. B.H. Bairamov, A. Heinrich, G. Irmer, V.V. Toporov, E. Ziegler, Phys. Status Solidi B **119**, 227 (1983)
37. F. Decremps, J. Pellicer-Porres, A.M. Saitta, J.C. Chervin, A. Polian, Phys. Rev. B **65**, 092101 (2002)
38. N. Ashkenov, B.N. Mbenkum, C. Bundesmann, V. Riede, M. Lorenz, E.M. Kaidashev, A. Kasic, M. Schubert, M. Grundmann, G. Wagner, H. Neumann, J. Appl. Phys. **93**, 126 (2003)
39. Y.F. Lu, H.Q. Ni, Z.M. Ren, W.J. Wang, T.C. Chong, T.S. Low, B.A. Cheng, J.P. Wang, Y.X. Jie, J. Laser Appl. **12**, 54 (2000)
40. J.N. Zeng, J.K. Low, Z.M. Ren, T. Liew, Y.F. Lu, Appl. Surf. Sci. **197–198**, 362 (2002)
41. J. Ye, S. Gu, S. Zhu, T. Chen, W. Liu, F. Qin, L. Hu, R. Zhang, Y. Shi, Y. Zheng, J. Vac. Sci. Technol. A **21**, 979 (2003)
42. J.D. Ye, S.L. Gu, S.M. Zhu, F. Qin, S.M. Liu, W. Liu, X. Zhou, L.Q. Hu, R. Zhang, Y. Shi, Y.D. Zheng, J. Appl. Phys. **96**, 5308 (2004)
43. C. Bundesmann, Ph.D. thesis, Universität Leipzig, 2005 (Shaker, Aachen, 2006)
44. C.X. Xu, X.Y. Sun, Jpn. J. Appl. Phys. **42**, 4949 (2003)
45. Y.J. Xing, Z.H. Xi, Z.Q. Xue, X.D. Zhang, J.H. Song, R.M. Wang, J. Xu, Y. Song, S.L. Zhang, D.P. Yu, Appl. Phys. Lett. **83**, 1689 (2003)
46. Y.K. Tseng, H.C. Hsu, W.F. Hsieh, K.S. Liu, I.C. Chen, J. Mater. Res. **18**, 2837 (2003)
47. H.Q. Ni, Y.F. Lu, Z.Y. Liu, H. Qiu, W.J. Wang, Z.M. Ren, S.K. Chow, Y.X. Jie, Appl. Phys. Lett. **79**, 812 (2001)
48. C. Bundesmann, N. Ashkenov, M. Schubert, D. Spemann, T. Butz, M. Lorenz, E.M. Kaidashev, M. Grundmann, Appl. Phys. Lett. **83**, 1974 (2003)
49. X. Wang, S. Yanga, J. Wanga, M. Lia, X. Jianga, G. Dua, X. Liub, R.P.H. Chang, J. Cryst. Growth **226**, 123 (2001)
50. A. Kaschner, U. Haboeck, M. Strassburg, M. Strassburg, G. Kaczmarczyk, A. Hoffmann, C. Thomsen, A. Zeuner, H.R. Alves, D.M. Hofmann, B.K. Meyer, Appl. Phys. Lett. **80**, 1909 (2002)
51. F. Reuss, C. Kirchner, T. Gruber, R. Kling, S. Maschek, W. Limmer, A. Waag, P. Ziemann, J. Appl. Phys. **95**, 3385 (2004)
52. M. Tzolov, N. Tzenov, D. Dimova-Malinovska, M. Kalitzova, C. Pizzuto, G. Vitali, G. Zollo, I. Ivanov, Thin Solid Films **379**, 28 (2000)
53. M. Tzolov, N. Tzenov, D. Dimova-Malinovska, M. Kalitzova, C. Pizzuto, G. Vitali, G. Zollo, I. Ivanov, Thin Solid Films **396**, 274 (2001)
54. Z. Zhaochun, H. Baibiao, Y. Yongqin, C. Deliang, Mater. Sci. Eng. B **86**, 109 (2001)
55. Z.Q. Chen, A. Kawasuso, Y. Xu, H. Naramoto, X.L. Yuan, T. Sekiguchi, R. Suzuki, T. Ohdaira, J. Appl. Phys. **97**, 013528 (2005)
56. Y.Q. Chang, D.B. Wang, X.H. Luo, X.Y. Xu, X.H. Chen, L. Li, C.P. Chen, R.M. Wang, J. Xu, D.P. Yu, Appl. Phys. Lett. **83**, 4020 (2003)
57. Y.Q. Chang, Y. Chen, D.P. Yu, Z.L. Fang, G.H. Li, F.H. Yang, Mater. Sci. Forum **475–479**, 3525 (2005)

58. J.B. Wang, H.M. Zong, Z.F. Li, W. Lu, J. Appl. Phys. **97**, 086105 (2005)
59. T.S. Jeong, M.S. Han, C.J. Youna, Y.S. Park, J. Appl. Phys. **96**, 175 (2004)
60. B. Cheng, Y. Xiao, G. Wu, L. Zhang, Appl. Phys. Lett. **84**, 416 (2004)
61. D. Zeng, C. Xie, B. Zhu, R. Jiang, X. Chen, W. Song, J. Wang, J. Shi, J. Cryst. Growth **266**, 511 (2004)
62. C. Bundesmann, M. Schubert, D. Spemann, T. Butz, M. Lorenz, E.M. Kaidashev, M. Grundmann, N. Ashkenov, H. Neumann, G. Wagner, Appl. Phys. Lett. **81**, 2376 (2002)
63. R.J. Collins, D.A. Kleinman, J. Phys. Chem. Solids **11**, 190 (1959)
64. E.C. Heltemes, H.L. Swinney, J. Appl. Phys. **38**, 2387 (1967)
65. E.F. Venger, A.V. Melnichuk, L.L. Melnichuk, Y.A. Pasechnik, Phys. Status Solidi B **188**, 823 (1995)
66. D.G. Thomas, J. Phys. Chem. Solids **10**, 47 (1959)
67. G. Heiland, H. Lüth, Solid State Commun. **5**, 199 (1967)
68. S. Perkowitz, R.K. Murty-Gutta, A.K. Garrison, Solid State Commun. **9**, 2251 (1971)
69. Z.C. Jin, I. Hamberg, C.G. Granquist, J. Appl. Phys. **64**, 5117 (1988)
70. A. Pflug, V. Sittinger, F. Ruske, B. Szyszka, G. Dittmar, Thin Solid Films **455–456**, 201 (2004)
71. C. Bundesmann, N. Ashkenov, M. Schubert, A. Rahm, H. v. Wenckstern, E.M. Kaidashev, M. Lorenz, M. Grundmann, Thin Solid Films **455–456**, 161 (2004)
72. C. Bundesmann, M. Schubert, D. Spemann, A. Rahm, H. Hochmuth, M. Lorenz, M. Grundmann, Appl. Phys. Lett. **85**, 905 (2004)
73. M. Schubert, *Infrared Ellipsometry on Semiconductor Layer Structures: Phonons, Plasmons and Polaritons* (Springer, New York, 2004)
74. C. Bundesmann, A. Rahm, M. Lorenz, M. Grundmann, M. Schubert, J. Appl. Phys. **99**, 113504 (2006)
75. Ü. Özgür, Y.I. Alivov, C. Liu, A. Teke, M.A. Reshchikov, S. Doğan, V. Avrutin, S.J. Cho, H. Morkoç, J. Appl. Phys. **98**, 041301 (2005)
76. H. Yoshikawa, S. Adachi, Jpn. J. Appl. Phys. **36**, 6237 (1997)
77. G.E. Jellison, Thin Solid Films **313–314**, 33 (1998)
78. P.L. Washington, H.C. Ong, J.Y. Dai, R.P.H. Chang, Appl. Phys. Lett. **72**, 3261 (1998)
79. X.W. Sun, H.S. Kwok, J. Appl. Phys. **86**, 408 (1999)
80. K. Postava, H. Sueki, M. Aoyama, T. Yamaguchi, C. Ino, Y. Igasaki, M. Horie, J. Appl. Phys. **87**, 7820 (2000)
81. R. Matz, H. Lüth, Appl. Phys. **18**, 123 (1979)
82. T.D. Kang, H. Lee, W.I. Park, G.C. Yib, Thin Solid Films **455–456**, 609 (2004)
83. G.E. Jellison, C.M. Rouleau, Appl. Opt. **44**, 3153 (2005)
84. Y.C. Liu, J.H. Hsieh, S.K. Tung, Thin Solid Films **510**, 32 (2006)
85. R. Schmidt-Grund, N. Ashkenov, M. M. Schubert, W. Czakai, D. Faltermeier, G. Benndorf, H. Hochmuth, M. Lorenz, and M. Grundmann, AIP Conf. Proc. **893**, 271 (2007).
86. G.J. Exarhos, A. Rose, C.F.W. Jr, Thin Solid Films **308–309**, 56 (1997)
87. Y.R. Park, K.J. Kim, Solid State Commun. **123**, 147 (2002)
88. H.E. Rhaleb, A.E. Naciri, R. Dounia, L. Johann, A. Hakam, M. Addou, Thin Solid Films **455–456**, 384 (2004)

89. A. Mendoza-Galvan, C. Trejo-Cruz, J. Lee, D. Bhattacharyya, J. Metson, P.J Evans, U. Pal, J. Appl. Phys. **99**, 014306 (2006)
90. J.H. Kang, Y.R. Park, K.J. Kim, Solid State Commun. **115**, 127 (2000)
91. R. Schmidt-Grund, M. Schubert, B. Rheinländer, D. Fritsch, H. Schmidt, E. Kaidashev, M. Lorenz, C. Herzinger, M. Grundmann, Thin Solid Films **455–456**, 500 (2004)
92. K.J. Kim, Y.R. Park, J. Appl. Phys. **91**, 1420 (2002)
93. K.J. Kim, Y.R. Park, J. Appl. Phys. **94**, 867 (2003)
94. K.J. Kim, Y.R. Park, J. Appl. Phys. **96**, 4150 (2004)
95. C.W. Teng, J.F. Muth, Ü. Özgür, M.J. Bergmann, H.O. Everitt, A.K. Sharma, C. Jin, J. Narayan, Appl. Phys. Lett. **76**, 979 (2000)
96. D. Zhao, Y. Liu, D. Shen, Y. Lu, J. Zhang, X. Fan, J. Cryst. Growth **234**, 427 (2002)
97. F.K. Shan, B.I. Kim, G.X. Liu, Z.F. Liu, J.Y. Sohn, W.J. Lee, B.C. Shin, Y.S. Yu, J. Appl. Phys. **95**, 4772 (2004)
98. I. Takeuchi, W. Yang, K.S. Chang, M.A. Aronova, T. Venkatesan, R.D. Vispute, L.A. Bendersky, J. Appl. Phys. **94**, 7336 (2003)
99. T. Minemoto, T. Negami, S. Nishiwaki, H. Takakura, Y. Hamakawa, Thin Solid Films **372**, 173 (2000)
100. J. Chen, W.Z. Shen, N.B. Chen, D.J. Qiu, H.Z. Wu, J. Phys. Condens. Matter **15**, L475 (2003)
101. M. Wraback, H. Shen, S. Liang, C.R. Gorla, Y. Lu, Appl. Phys. Lett. **74**, 507 (1999)
102. C.R. Gorla, N.W. Emanetoglu, S. Liang, W.E. Mayo, Y. Lu, M. Wraback, H. Shen, J. Appl. Phys. **85**, 2595 (1999)
103. S. Muthukumar, J. Zhong, Y. Chen, Y. Lu, T. Siegrist, Appl. Phys. Lett. **82**, 742 (2003)
104. B.P. Zhang, Y. Segawa, K. Wakatsuki, Y. Kashiwaba, K. Haga, Appl. Phys. Lett. **79**, 3953 (2001)
105. E. Ruiz, S. Alvarez, P. Alemany, Phys. Rev. B **49**, 7115 (1994)
106. K. Thoma, B. Dorner, G. Duesing, W. Wegener, Solid State Commun. **15**, 1111 (1974)
107. A.W. Hewat, Solid State Commun. **8**, 187 (1970)
108. A. Seko, F. Oba, A. Kuwabara, I. Tanaka, Phys. Rev. B **72**, 024107 (2005)
109. A. Anderson (ed.), *The Raman Effect, Vol. 2: Applications* (Marcel Dekker, New York, 1973)
110. R.H. Lyddane, R.G. Sachs, E. Teller, Phys. Rev. **59**, 673 (1941)
111. C.M. Wolfe, N. Holonyak, G.E. Stillmann, *Physical Properties of Semicoductors* (Prentice Hall, New Jersey, 1989)
112. P. Yu, M. Cardona, *Fundamentals of Semiconductors* (Springer, Berlin, 1999)
113. S. Adachi, *GaAs and Related Materials* (World Scientific, New Jersey, 1994)
114. R.M.A. Azzam, N.M. Bashara, *Ellipsometry and Polarized Light* (North-Holland, Amsterdam, 1977)
115. A. Rössler, *Infrared Spectroscopic Ellipsometry* (Akademie-Verlag, Berlin, 1990)
116. H.G. Tompkins, W.A. McGahan, *Spectroscopic Ellipsometry and Reflectometry: A User's Guide* (Wiley, New York, 1999)
117. H.G. Tompkins, E.A. Irene (eds.), *Handbook of Ellipsometry* (William Andrew Publishing, Highland Mills, 2004)

118. H. Fujiwara, Spectroscopic Ellipsometry: Principles and Applications (John Wiley & Sons Ltd, Chichester, 2007)
119. M. Schubert, Phys. Rev. B **53**, 4265 (1996)
120. M. Schubert, T. Hofmann, C.M. Herzinger, J. Opt. Soc. Am. A **20**, 347 (2003)
121. G.E. Jellison, L.A. Boatner, Phys. Rev. B **58**, 3586 (1998)
122. M. Rebien, W. Henrion, M. Bär, C.H. Fischer, Appl. Phys. Lett. **80**, 3518 (2002)
123. M. Schubert, T.E. Tiwald, C.M. Herzinger, Phys. Rev. B **61**, 8187 (2000)
124. W.L. Bond, J. Appl. Phys. **36**, 1674 (1965)
125. S.P.S. Porto, R.S. Kishnan, J. Chem. Phys. **47**, 1009 (1967)
126. G.H. Watson, W.B. Daniels, C.S. Wang, J. Appl. Phys. **52**, 956 (1981)
127. D.G. Mead, G.R. Wilkinson, J. Raman Spectrosc. **6**, 123 (1977)
128. J.B. Cui, K. Amtmann, J. Ristein, L. Ley, J. App. Phys. **83**, 7929 (1998)
129. L. Viña, S. Logothetidis, M. Cardona, Phys. Rev. B **30**, 1979 (1984)
130. S.S. Mitra, O. Brafman, W.B. Daniels, R.K. Crawford, Phys. Rev. **186**, 942 (1969)
131. F.J. Manjón, B. Marí, J. Serrano, A.H. Romero, J. App. Phys. **97**, 053516 (2005)
132. J. Chen, W.Z. Shen, Appl. Phys. Lett. **83**, 2154 (2003)
133. J.R. Jasperse, A. Kahan, J.N. Plendl, S.S. Mitra, Phys. Rev. **146**, 516 (1966)
134. J. Serrano, A.H. Romero, F.J. Manjón, R. Lauck, M. Cardona, A. Rubio, Phys. Rev. B **69**, 094306 (2004)
135. E. Mollwo, R. Till, Zeitschrift für Physik **216**, 315 (1968)
136. R. Synowicki, T.E. Tiwald, Thin Solid Films **455–456**, 248 (2004)
137. E. Mollwo, Z. Angew. Phys. **6**, 257 (1954)
138. W.S. Hu, Z.G. Liu, J. Sun, S.N. Zhu, Q.Q. Xu, D. Feng, Z.M. Ji, J. Phys. Chem. Solids **58**, 853 (1997)
139. N.B. Chen, H.Z. Wu, T.N. Xu, J. Appl. Phys. **97**, 023515 (2005)
140. E.D. Palik (ed.), *Handbook of Optical Constants of Solids*, vol. 3 (Academic Press, New York, 1998)
141. C.F. Klingshirn, *Semiconductor Optics* (Springer, Berlin, 1997)
142. J.F. Muth, R.M. Kolbas, A.K. Sharma, S. Oktyabrsky, J. Narayan, J. Appl. Phys. **85**, 7884 (1999)
143. A. Djurisic, Y. Chan, E. Li, Appl. Phys. A **76**, 37 (2003)
144. S. Ozaki, T. Mishima, S. Adachi, Jpn. J. Appl. Phys. **42**, 5465 (2003)
145. V. Srikant, D.R. Clarke, J. Appl. Phys. **81**, 6357 (1997)
146. S.A. Studenikin, N. Golego, M. Cocivera, J. Appl. Phys. **83**, 2104 (1998)
147. F.D. Paraguay, W.L. Estrada, D.R.N. Acosta, E. Andrade, M. Miki-Yoshida, Thin Solid Films **350**, 192 (1999)
148. X.Q. Meng, W. Zhen, J.P. Guo, X.J. Fan, Appl. Phys. A **70**, 421 (2000)
149. G. Santana, A. Morales-Acevedo, O. Vigil, L. Vaillant, F. Cruz, G. Contreras-Puente, Thin Solid Films **373**, 235 (2000)
150. M.S. Tokumoto, A. Smith, C.V. Santilli, S.H. Pulcinelli, A.F. Craievich, E. Elkaim, A. Traverse, V. Briois, Thin Solid Films **416**, 284 (2002)
151. F.K. Shan, Y.S. Yu, Thin Solid Films **435**, 174 (2003)
152. P. Misra, P. Sahoo, P. Tripathi, V. Kulkarni, R. Nandedkar, L. Kukreja, Appl. Phys. A **78**, 37 (2004)
153. J.L. Zhao, X.M. Li, J.M. Bian, W.D. Yu, X.D. Gao, J. Cryst. Growth **276**, 507 (2005)

154. B. Segall, Phys. Rev. **163**, 1674 (1967)
155. S.L. Chuang, C.S. Chang, Phys. Rev. B **54**, 4005 (1970)
156. T. Kawashima, H. Yoshikawa, S. Adachi, S. Fuke, K. Ohtsuka, J. Appl. Phys. **82**, 3528 (1997)
157. D.C. Reynolds, D.C. Look, B. Jogai, C.W. Litton, T.C. Collins, M.T. Harris, M.J. Callahan, J.S. Bailey, J. Appl. Phys. **86**, 5598 (1999)
158. B. Gil, Phys. Rev. B **64**, R201310 (2001)
159. J.J. Hopefield, J. Phys. Chem. Solids **15**, 97 (1960)
160. L.C. Lew Yan Voon, M. Willatzen, M. Cardona, N.E. Christensen, Phys. Rev. B **53**, 10703 (1996)
161. W.Y. Liang, A.D. Yoffe, Phys. Rev. Lett. **20**, 59 (1968)
162. D.W. Langer, R.N. Euwema, K. Era, T. Koda, Phys. Rev. B **2**, 4005 (1970)
163. D.C. Reynolds, D.C. Look, B. Jogai, C.W. Litton, G. Cantwell, W.C. Harsch, Phys. Rev. B **60**, 2340 (1999)
164. A. Mang, K. Reimann, S. Rübenacke, Solid State Commun. **94**, 251 (1995)
165. Y.P. Varshni, Physica **34**, 149 (1967)
166. K.P. O'Donnel, X. Chen, Appl. Phys. Lett. **58**, 2924 (1991)
167. C. Boemare, T. Monterio, M.J. Soares, J.G. Guilherme, E. Alves, Physica B **308–310**, 985 (2001)
168. L. Wang, N.C. Giles, J. Appl. Phys. **94**, 973 (2003)
169. R. Pässler, J. Appl. Phys. **89**, 6235 (2001)
170. A. Manoogian, A. Leclerc, Can. J. Phys. **57**, 1766 (1979)
171. J.M. Zhang, T. Ruf, R. Lauck, M. Cardona, Phys. Rev. B **57**, 9716 (1998)
172. A. Göbel, T. Ruf, J.M. Zhang, R. Lauck, M. Cardona, Phys. Rev. B **59**, 2749 (1998)
173. R. Pässler, Phys. Status Solidi B **216**, 975 (1999)
174. S.V. Mel'nichuk, V.I. Sokolov, T.P. Surkova, V.M. Chernov, Sov. Phys. Solid State **33**, 1833 (1991)
175. S. Serrano, F. Widulle, A.H. Romero, A. Rubio, R. Lauck, M. Cardona, Phys. Status Solidi B **235**, 260 (2003)
176. R. Pässler, E. Griebl, H. Riepl, G. Lauther, S. Bauer, H. Preis, W. Gebhardt, B. Buda, D.J. As, D. Schikora, K. Lischka, K. Papagelis, S. Ves, J. Appl. Phys. **86**, 4403 (1999)
177. P. Lautenschlager, M. Garriga, S. Logothetidis, M. Cardona, Phys. Rev. B **35**, 9174 (1987)
178. H. Watanabe, M. Wada, T. Takahashi, Jpn. J. Appl. Phys. **3**, 617 (1964)
179. J.E. Jaffe, R. Pandey, A.B. Kunz, Phys. Rev. B **43**, 14030 (1991)
180. G.E. Jellison, Phys. Rev. B **65**, 049902 (2001)